

**LITHOSPHERIC STRUCTURE BENEATH NORTHERN MISSISSIPPI  
EMBAYMENT FROM JOINT INVERSION OF  
SURFACE WAVE DISPERSION AND  
RECEIVER FUNCTIONS**

Han Su, B. S.

A Thesis Presented to the Graduate Faculty of Saint Louis University  
in Partial Fulfillment of the Requirements for  
the Degree of Master of Science

2015

COMMITTEE IN CHARGE OF CANDIDACY:

Professor Robert Herrmann,  
Chairperson and Advisor

Professor Lupei Zhu

Professor John Encarnación

## ACKNOWLEDGEMENT

During the past two years, I've received a lot of help from the professors and my fellow classmates of the Earth and Atmospheric Sciences Department in Saint Louis University. Here I'd like to express my gratitude to them.

First, I'd like to thank my supervisor Dr. Robert Herrmann, who brought this thesis topic to me at the second semester of my Master program. He has always been very patient and generous in sharing his invaluable time and knowledge. He put a great effort into guiding me and revising my thesis manuscript. Without him, I couldn't have finished this project and this manuscript. I also appreciate the suggestion and opportunity he gave me to attend the Seismological Society of America (SSA) 2014 annual meeting and present this study as a poster. His devotion and achievement to seismology and education deserve my greatest admiration.

I'm also very thankful to my other committee members, Dr. Lupei Zhu and Dr. John Encarnación. Dr. Zhu gave me many advices when I practiced my thesis defense at the end of my forth semester. The suggestions and questions they brought up during my defense are very useful and worthy to be penetratingly explored.

I appreciate Dr. Charles J. Ammon for providing his tomographic inversion program and National Science Foundation (NSF) for supporting me to accomplish this research.

I'm grateful to all the professors in this department, Dr. David Crossley and Dr. Linda Warren, for preparing those wonderful lectures for us and solving all the problems we had in the coursework. I've learned and improved a lot in not only knowledge of seismology but also the skill in public presentation.

I appreciate my fellow classmate, Hao Guo, for helping me with a lot of work of my research such as picking dispersion curves and running inversion programs.

I'd like to thank all my fellow classmates as well, especially Jiahao Liang, Ying Chang, Jiashu Song, Wanying Wang and Junxi Miao, for helping me a lot in my both academic and personal life. I appreciate the delicious food they cooked and I want to thank Jiashu Song for letting me stay at her apartment during her absence these days. We've become good friends more than classmates for the past two years and I'll treasure our friendship forever.

In the end, I'd like to thank my parents for their unconditional love and support. They've always been proud of me and I really appreciate it.

I've spent an amazing time studying at Saint Louis University. I believe the wonderful experience and the nice professors and friends I've met and made here will make me a better person in the future.

## TABLE OF CONTENTS

List of Figures.....	v
CHAPTER 1: INTRODUCTION.....	1
Geological background.....	1
Seismicity.....	3
Statement of the Problem.....	4
CHAPTER 2: LITERATURE REVIEW.....	5
The objective of this study.....	14
CHAPTER 3: METHODOLOGY.....	15
Surface wave analysis.....	15
Rayleigh wave and Love wave.....	15
Dispersion.....	17
Phase velocity and group velocity.....	17
Equations of motion for elastic medium.....	18
Eigenfunction of surface waves.....	20
Ambien noise tomography (ANT).....	22
Multiple Filter Analysis (MFT).....	23
Least-square tomographic inversion.....	25
Receiver function.....	28
Joint inversion.....	30
Model test.....	31
CHAPTER 4: DATA.....	33
CHAPTER 5: RESULTS AND DISCUSSION.....	35
Dispersion maps.....	35
Checkerboard test.....	35
Real data result.....	39
Dispersion curves comparison.....	40
1D Velocity maps.....	44
2D Velocity profiles.....	52
Model test.....	56
CHAPTER 6: CONCLUSION.....	63
References.....	64
Vita Auctoris.....	75

## LIST OF FIGURES

Figure 1:	Geologic map of North America (Reed et al., 2004).....	1
Figure 2:	Location of northern and central Mississippi Embayment (Cushing et al., 1964, pg. B2).....	2
Figure 3:	Geological setting and seismicity in northern ME.....	3
Figure 4:	Gray-shaded Bouguer gravity anomaly map of the upper Mississippi Embayment region (Hildenbrand, 1985, pg. 12612).....	6
Figure 5:	Gray-shaded residual aeromagnetic map of the upper Mississippi Embayment region (Hildenbrand, 1985, pg. 12610).....	6
Figure 6:	Reference map of the northern Mississippi Embayment region (Hildenbrand and Hendricks, 1995, pg. E2).....	7
Figure 7:	Configuration of the Paleozoic-Cretaceous unconformity (Stearns and Marcher, 1962, pg. 1388).....	8
Figure 8:	Crustal velocity model of the Mississippi Embayment (Mooney, 1983, pg. 344).....	9
Figure 9:	The P-wave crustal velocity model of Mooney and Andrews (1984) (Chiu et al., 1992, pg. 379) .....	11
Figure 10:	Particle motion of Rayleigh wave (Lowrie, 2007, pg. 136).....	16
Figure 11:	Particle motion of Love wave (Lowrie, 2007, pg. 137).....	16
Figure 12:	Dispersive surface waves at increasing distances and times .....	18
Figure 13:	Least-square inversion grids.....	26
Figure 14:	Receiver function ray diagram (Ammon et al., 1990, pg. 15304).....	29
Figure 15:	Receiver function trace (Ammon et al., 1990, pg. 15304).....	29
Figure 16:	Distribution of TA stations around the northern ME.....	33
Figure 17:	Synthetic surface wave velocity model .....	36
Figure 18:	Checkerboard test for Love wave phase velocity dispersion maps at 3, 6, 12, 24 s .....	37
Figure 19:	Checkerboard test for Rayleigh wave phase velocity dispersion maps at 3, 6, 12, 24 s .....	38
Figure 20:	Love wave phase velocity dispersion maps at 3, 6, 12, 24 s .....	39
Figure 21:	Rayleigh wave phase velocity dispersion maps at 3, 6, 12, 24 s .....	40

Figure 22:	Comparison of Love/Rayleigh phase/group dispersion at (36N, 91W).....	42
Figure 23:	Comparison of Love/Rayleigh phase/group dispersion at (37N, 89W).....	43
Figure 24:	1D shear wave velocity models at depth of 0-240km .....	45
Figure 25:	Velocity model and dataset before joint inversion under station W44A .....	47
Figure 26:	Velocity model and dataset after joint inversion under station W44A .....	48
Figure 27:	Velocity model and dataset before joint inversion under station S43A .....	50
Figure 28:	Velocity model and dataset after joint inversion under station S43A .....	51
Figure 29:	2D Velocity profile lines .....	53
Figure 30:	2D east-west velocity profiles .....	54
Figure 31:	2D velocity profiles paralleling the axis of embayment.....	56
Figure 32:	Model test map .....	57
Figure 33:	Models used for synthetics computation .....	58
Figure 34:	Waveform pattern comparison for station S43A .....	60
Figure 35:	Waveform pattern comparison for station Q42A.....	62

## CHAPTER 1: INTRODUCTION

### 1.1 Geological background

From the geologic map of North America [Reed et al., 2004] (see Figure 1), Mississippi Embayment (ME) is the region recognized as one of the major first-order geological structures in the central U.S. [Cox and Van Arsdale, 2002]. It covers the area of over 100,000 square miles in the Gulf Coastal Plain [Cushing et al., 1964].



Figure 1: Geologic map of North America (Reed et al., 2004)

Starting from the junction of Missouri, Illinois and Kentucky and with its axis roughly aligning with the current Mississippi River channel, the northern embayment is characterized by a SSW-plunging trough filled with unconsolidated Late Cretaceous and Cenozoic alluvial sediments. Underlying the sediments is the Reelfoot rift composed of Paleozoic bedrocks [Stearns, 1957; Cushing et al., 1964; Mooney, 1983]. The thicknesses of the sediments in the embayment are variable and exhibit a wedge shape from a 3-D perspective. The sediments get thinner towards the edges in the direction perpendicular to the axis of the embayment

[Hinze and Braile, 1988]. Along the axis, the depth of sediments can reach 500 m at New Madrid, Missouri and 1000 m near Memphis, Tennessee [Van Arsdale and TenBrink, 2000].

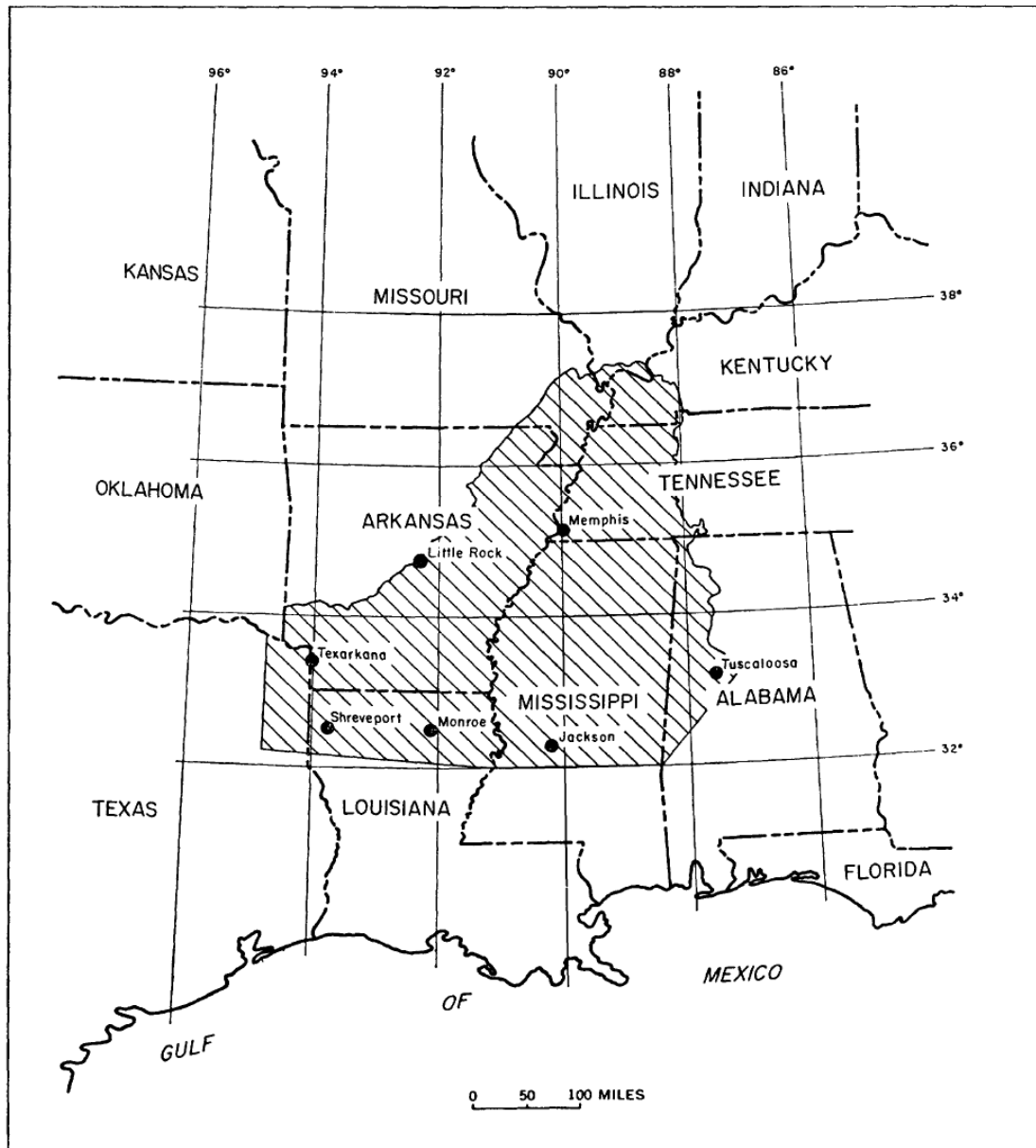


Figure 2: Location of northern and central Mississippi Embayment (Cushing et al., 1964, pg. B2)

*Note.* The dash dot lines are state boundaries; the shaded area is the study area of the published paper by Cushing et al., 1964; large cities inside this area are marked as black dots.

New Madrid Seismic Zone (NMSZ) is a 70-km-wide, 200-km-long strike-slip fault zone in the upper crust of northern embayment [Pollitz and Mooney, 2014] (see Figure 3). Main tectonic features around the northern embayment are shown in Figure 3, such as the

Illinois Basin in the north, the Ouachita Mountains in the southwest and the Nashville Dome in the east. The Appalachian-Ouchita orogenic belts are formed by continent-continent collision in Paleozoic [Hatcher, 1989]. To the north of this convergent margin is a divergent belt beneath the NMSZ, called the Reelfoot rift [Ervin and McGinnis, 1975].

## 1.2 Seismicity

Over the past two centuries, the northern embayment has always been affected by high seismicity, especially inside the NMSZ. As the most active seismic zone in central United States, NMSZ generated a series of catastrophic earthquakes with magnitudes larger than 7 in 1811-1812 [Johnston and Schweig, 1996]. These events are regarded as the unprecedentedly largest earthquakes in the U.S. at that time [Nuttli, 1973]. Based on a report completed by the Mid America Earthquake Center, a magnitude 7.7 earthquake occurring in the NMSZ can cause an estimated direct economic loss of 300 billion dollars [Elnashai et al., 2009].

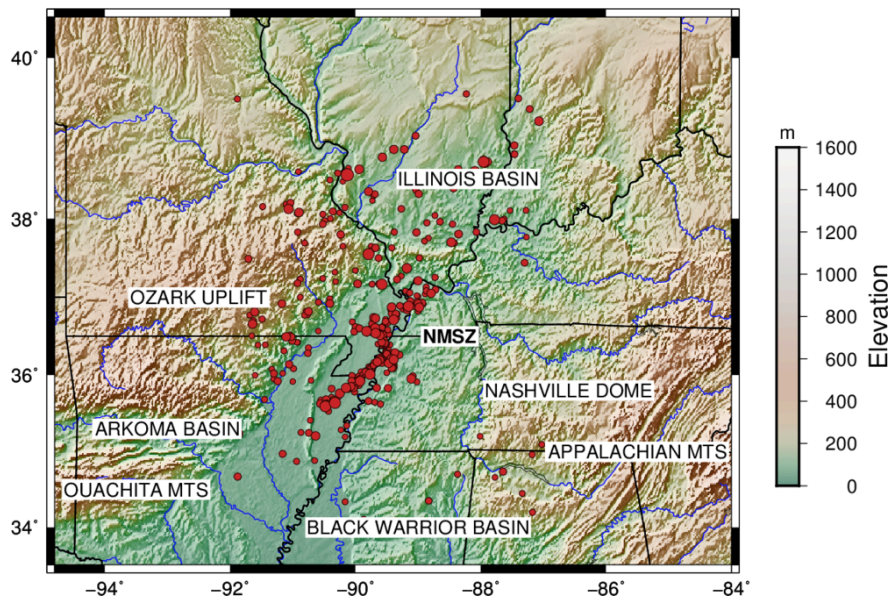


Figure 3: Geological setting and seismicity in northern ME

*Note.* The elevation of this area is indicated in colors. Main features are marked surrounding the New Madrid Seismic Zone (NMSZ). Earthquakes that occurred between 01/1973 and 03/2015 with magnitude larger than 2.5 are shown in solid red circles. The symbol size is proportional to the magnitude of each event.

Data source: the topography data is extracted from ETOPO1 Global Relief Model [Amante and Eakins, 2009]; the labeled tectonic features are based on the tectonic diagram in the Quaternary Geology of the Lower Mississippi Valley [Saucier and Snead, 1989]; earthquake events are downloaded from U.S. Geological Survey (USGS) website.

The occurrence of microearthquakes also remains a high rate in the northern embayment [Andrews et al., 1984; Bisrat et al., 2012]. In addition, paleoliquefaction investigations provide convincing evidence for historical large earthquakes in about 1450 and 900 A.D. and even 3500 and 4800 B.C. [Tuttle et al., 2002, 2006].

All these peculiar characteristics define the NMSZ as one of the most important seismic zones for an intraplate seismicity study [Johnston and Schweig, 1996; Liang and Langston, 2008].

### **1.3 Statement of the Problem**

Since thick sediments have filled the major ancient rift, high-quality geophysical data are not easy to obtain in this region. This unavailability limits our understanding of the buried structures, which may be able to explain the anomalous seismicity [Johnston and Schweig, 1996; Liang and Langston, 2008]. As a result, although many studies have focused on the specific earthquakes or the structure at specific locations in the NMSZ, there has no consensus on the mechanism for the unique seismic behavior in this region. Different models for the anomalously active seismic zone have been proposed [Ervin and McGinnis, 1975; Kane et al., 1981; Cox and Van Arsdale, 1997, 2002; Forte et al., 2007], but none of them can tell a perfect story or is widely accepted.

Recently, it's been proposed that the structural heterogeneity in the lithosphere under the northern embayment may serve as the dominant control factor for the formation of NMSZ [Pollitz and Mooney, 2014]. To help unveil the buried structural secrets of this area, there is a need for a high-resolution velocity model for the region.

## CHAPTER 2: LITERATURE REVIEW

Efforts have been made by geologists and geophysicists in the search for the crustal and mantle structure information within the northern Mississippi Embayment. Various investigations have been conducted that acquired different types of datasets and used different methods for data processing and interpretation.

Potential field investigations provide a valid solution to understand the subsurface structure beneath the thick sedimentary sequences covering the surface of the embayment. In 1974, the U.S. Geological Survey (USGS) initiated gravity and aeromagnetic surveys in the northern Embayment, trying to find a structure that may attribute to the local seismicity. Bouguer gravity and magnetic anomaly maps for this region were plotted and then interpreted. [Hildenbrand and Johnson, 1977; Hildenbrand et al., 1977a, 1977b, 1982; Kane et al., 1981; Hildenbrand, 1985]. In the gravity anomaly maps, an anomalous high-density lower crust, which was reflected by regional positive gravity anomalies, was identified inside the embayment (see Figure 4). High magnetic anomalies were detected not only at the rift boundaries but also within the embayment parallel to the axis of the rift (see Figure 5). The magnetic anomaly map suggested the mantle material was intruded along faults formed in a weak shear zone [Hildenbrand, 1985]. Both magnetic and gravity data drafted the delineation of the buried Reelfoot rift, the host structure of the NMSZ, and indicated a long and complex interaction of tectonic and magmatic activities [Hildenbrand and Hendricks, 1995] (see Figure 6). Information about the configurations and depths of Paleozoic surface and Precambrian basement were provided by contour and subcrop maps [Stearns and Marcher, 1962; Dart, 1995] (see Figure 7).

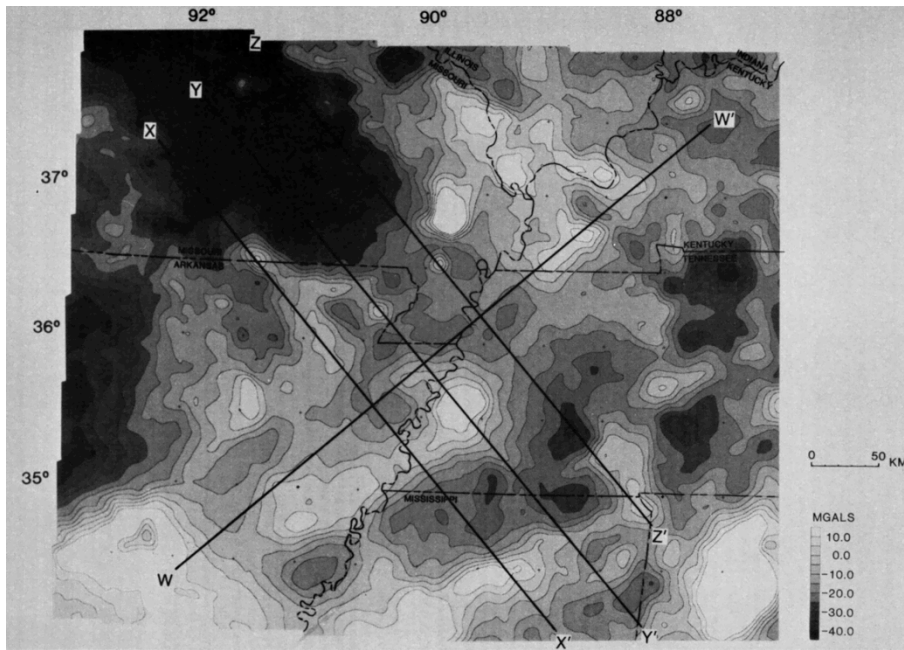


Figure 4: Gray-shaded Bouguer gravity anomaly map of the upper Mississippi Embayment region (Hildenbrand, 1985, pg. 12612)

*Note.* Reduction density =  $2.67 \text{ g/cm}^3$ ; profile lines X-X', Y-Y', Z-Z' and W-W' are for the published paper by Hildenbrand, 1985.

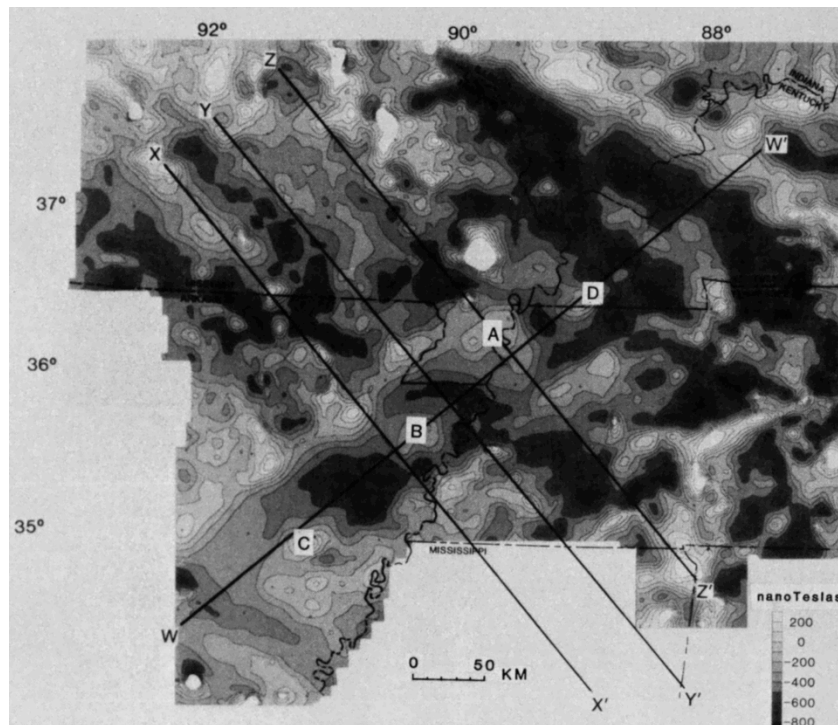
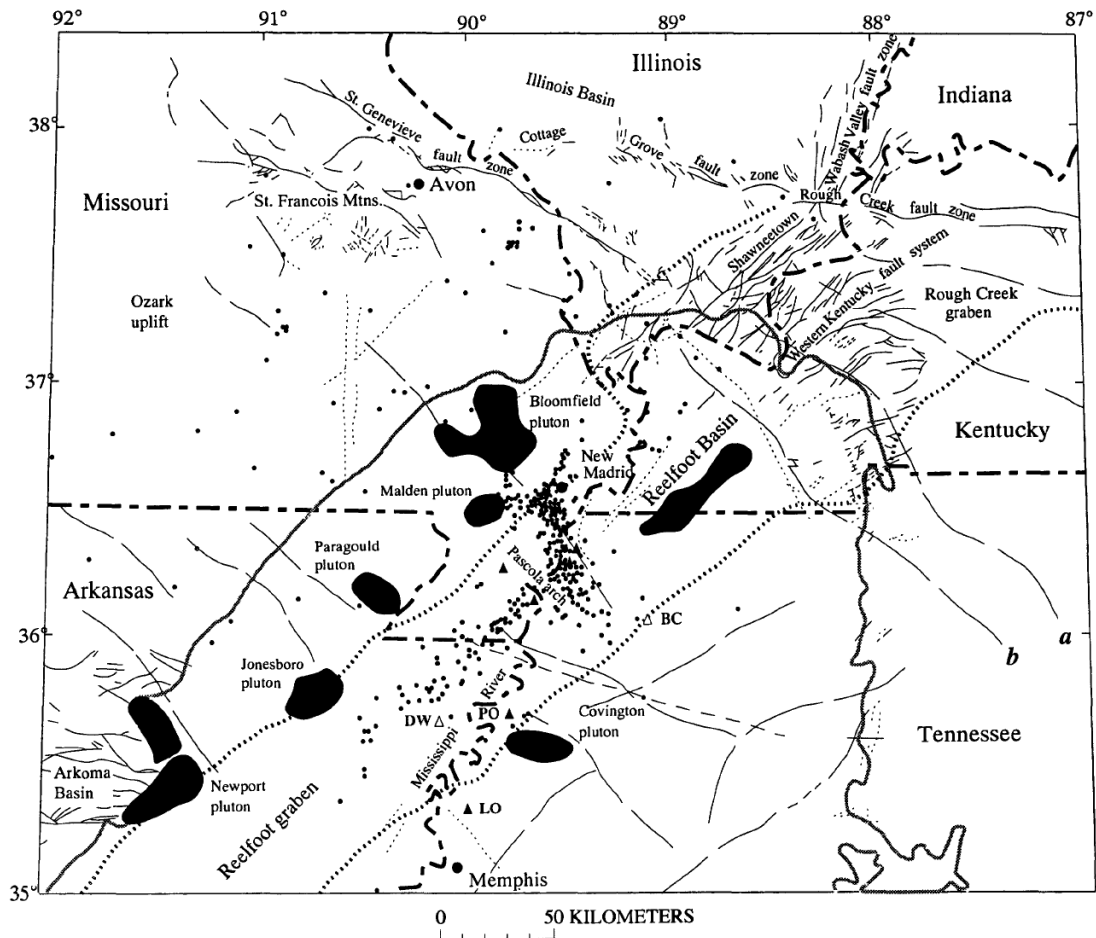


Figure 5: Gray-shaded residual aeromagnetic map of the upper Mississippi Embayment region (Hildenbrand, 1985, pg. 12610)

*Note.* Upper case letters (A, B, C, D) denote locations of magnetic anomalies associated with igneous bodies within the graben; profile lines X-X', Y-Y', Z-Z' and W-W' are for the published paper by Hildenbrand, 1985.



EXPLANATION	
<p>— Northern limit of coastal-plain material of the Mississippi Embayment</p> <p>▲ Mafic or ultramafic intrusions within the Mississippi Embayment identified in drill-hole cuttings. Intrusions labeled PO and LO are also locations of the Pure Oil McGregor No. 1 and the Lion Oil Company No. 1 wells, respectively</p> <p>● Mafic intrusion within the Mississippi Embayment interpreted from the magnetic field. Approximate boundaries of intrusions determined from zero contour of associated anomaly on a second vertical derivative map</p> <p>● City or town</p>	<p>— Long dashed lines show principal magnetic lineaments reflecting faulting and lithologic contrasts in magnetic basement. <i>a</i> and <i>b</i> are lineaments discussed in text</p> <p>— Fault - Dashed where inferred</p> <p>..... Possible or hypothetical fault. Locations based on subsurface data or exceptionally strong lineaments from aerial photographs</p> <p>..... Approximate margins of the Reelfoot graben</p> <p>△ Locations of the Big Chief (BC) and Dow Chemical 1 Wilson (DW) drill holes</p> <p>● Earthquake epicenter</p>

Figure 6: Reference map of the northern Mississippi Embayment region (Hildenbrand and Hendricks, 1995, pg. E2)

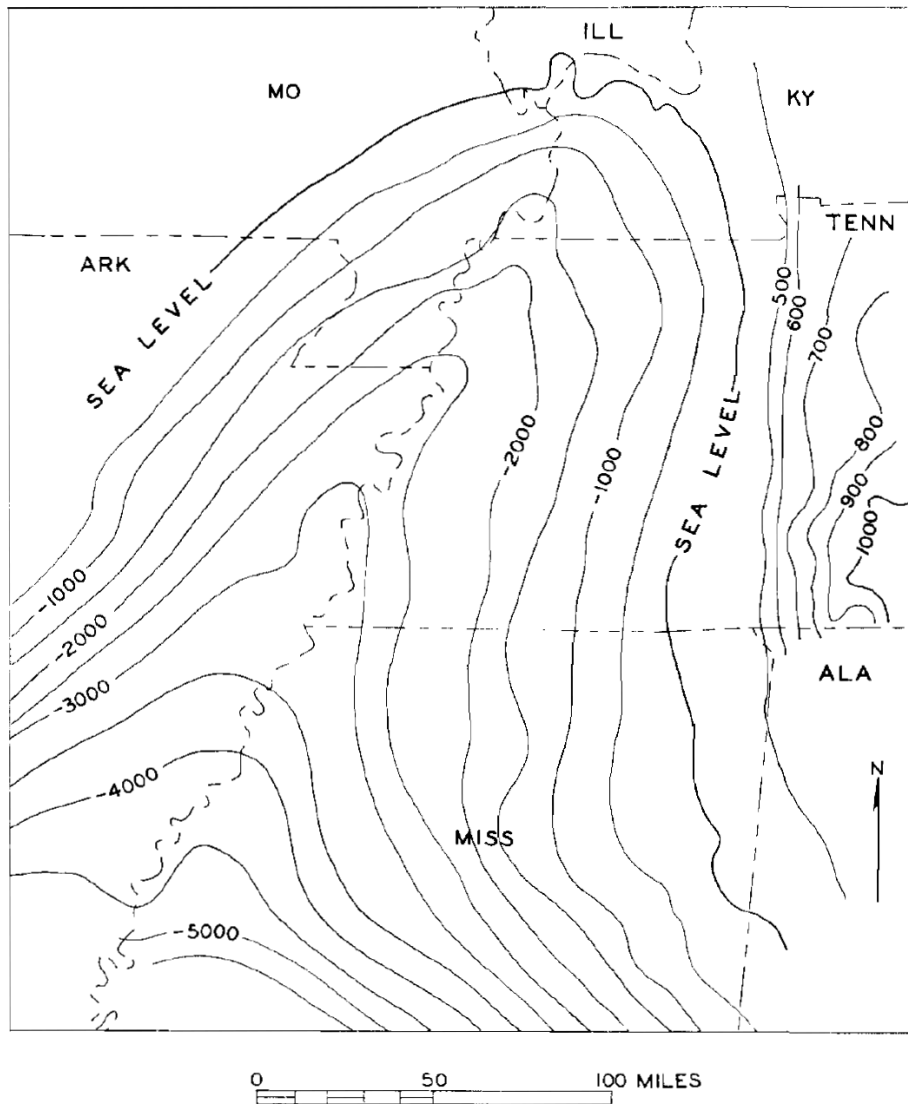


Figure 7: Configuration of the Paleozoic-Cretaceous unconformity (Stearns and Marcher, 1962, pg. 1388)

*Note.* The thin uppermost sediment layer and the low-velocity layer emphasized in the text are darkened. S-wave velocities were added to this model by Andrews et al. (1985) by assuming  $V_p = 1.73V_s$

Together with available logging, gravity and magnetic data, seismic profiles produced from refraction/reflection experiments conducted in the northern ME enable a more detailed vision of the underground configuration [Ginsburg et al., 1983; Mooney et al., 1983; Nelson and Zhang, 1991; Catching, 1999]. In September 1980, a series of refraction profiles were collected by USGS in different directions across the rift zone within the northern embayment. By analyzing the recorded refraction data, Mooney et al. [1983] proposed a 6-layer 1D model

including the crust with velocities ranging from 1.8 km/s to 7.3 km/s and the uppermost mantle with the velocity of 8 km/s up to 50 km (see Figure 8). In this model, the uppermost layer was composed of 0.65 km-thick unconsolidated Cretaceous and Cenozoic sediments and there is a 2.5 km-thick low-velocity zone (4.9 km/s) existing in the middle of the upper crust. The low velocity zone separated the Paleozoic carbonate and clastic sedimentary rocks (5.9 km/s) from the Precambrian crystalline basement rocks (6.2 km/s in the upper crust and 6.6 km/s in the lower crust), and was interpreted to be Early Paleozoic sediments (probably marine shale) deposited after rifting. An anomalous doming high-velocity layer (7.3 km/s) was found between the 6.6 km/s lower crust and 8 km/s upper mantle. It thins to the east, west and southwest directions, and could represent intruded mantle plumes related to the rifting. Faults and igneous intrusions were identified with better precision in reflection sections across the seismic zone, which also showed consistency with previous magnetic data [Zoback et al., 1980; Braile et al., 1986].

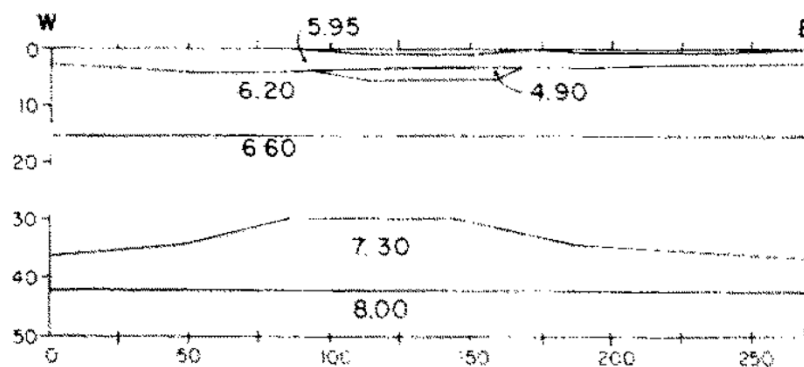


Figure 8: Crustal velocity model of the Mississippi Embayment (Mooney, 1983, pg. 344)

*Note.* Depth and length units are km; velocity unit is km/s; the most top layer has the velocity of 1.8 km/s.

Earthquakes themselves, which act as one of the major impetuses of all geological and geophysical investigations and interpretations, also provide a good opportunity to access

the information of subsurface structure [Herrmann and Fisher, 1978]. The first seismograph to record seismic events in this region was installed at Saint Louis University in 1909. Since 1974, the USGS began to support a systematic local seismic network in the NMSZ, called the Central Mississippi Valley Seismic Network (CMVSN), for the purpose of earthquake monitoring. This local network was upgraded in 1990 and then named the Cooperative New Madrid Seismic Network (CNMSN) [Shedlock and Johnston, 1994]. Short-term arrays have also been deployed in the NMSZ such as the Portable Array for Numerical Data Acquisition (PANDA) project designed by the Center for Earthquake Research and Information (CERI), Memphis State University from 1989 through 1992 [Chiu et al., 1991]. With the ongoing deployment of the Transportable Array (TA) of EarthScope Project, the northern ME has been covered by high quality 3-component broadband seismometers with an interstation spacing of about 70 km [Long et al., 2014]. Local earthquakes and teleseismic events have been monitored and recorded in the northern embayment for more than four decades, and the epicenter pattern for this region has been revealed more clearly [Braile et al., 1997].

A 1-D crustal model for the NMSZ was presented by Chiu et al. [1992] after independent P- and S-velocity inversions with travel time information recorded from PANDA and using well log data as constraints. Their new model basically agreed with previous models proposed by Mooney et al. [1983] and Mooney and Andrews [1984] from refraction measurements (see Figure 9), but a low P-wave/S-wave velocity ratio was given for the low velocity zone in the upper crust. The possible explanation for the low value could be the low P-velocity of the sedimentary composition (shale) and the elevated S-velocity caused by high pore fluid pressure and fluid-filled fractures.

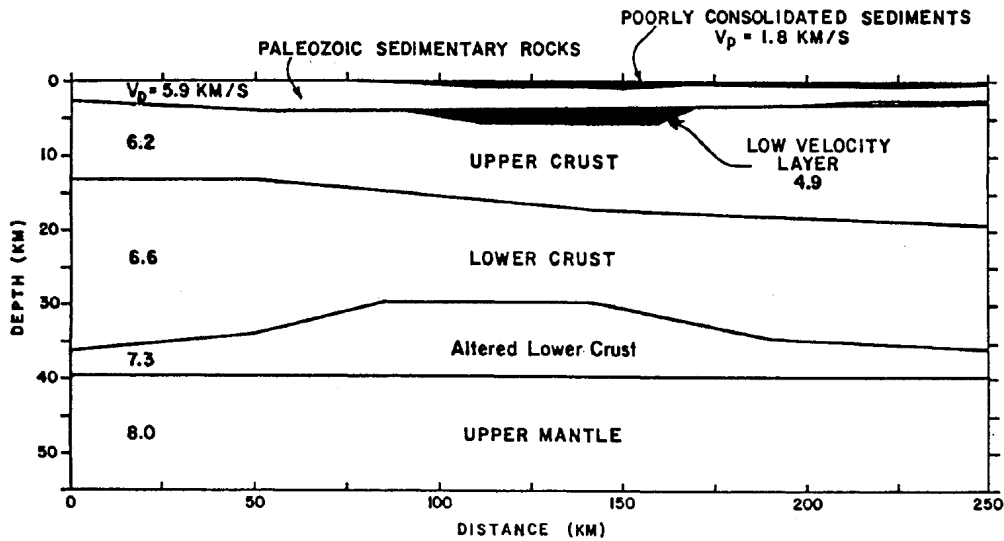


Figure 9: The P-wave crustal velocity model of Mooney and Andrews (1984) shown in east-west profile through the study area (Chiu et al., 1992, pg. 379)

3-D P- and S-wave crustal velocity structures in the NMSZ were modeled using local earthquake data and refined with higher resolution and broader spatial scope [Al-Shukri and Mitchell, 1988; Vlahovic et al., 2000; Vlahovic and Powell, 2001; Powell et al., 2010; Dunn et al. 2013]. Al-Shukri and Mitchell [1988] performed the P-wave arrival time inversion from local network data (CNMSN). Their resulting single-layer and two-layer upper crustal P-wave velocity models both showed a good match between the range of the lowest velocity region and the high seismicity zone. Vlahovic et al. [2000] and Vlahovic and Powell [2001] used a nonlinear travel time tomography method with the dataset from PANDA to obtain 3-D P- and S-wave velocity models for the crustal structure of the NMSZ. The grid size for both velocity models is  $4\text{km} \times 4\text{km}$  in the horizontal plane, and good resolution can be obtained to the depth of 11 km for the P-velocity model and 10 km for the S-velocity model. In addition to the coincident distribution of the low velocities and dense seismic events, their also found that the low velocity region didn't correspond to the low density shown in the gravity map very well, and therefore high pore pressure and intense fracturing of the underlying layer could be responsible for the low velocities. For the high velocity anomalies in the model, the

ones found parallel to the rift margins were considered to be due to the Precambrian crystalline rocks and the small-scale high velocity regions were interpreted together with gravity and magnetic data to be basaltic intrusions. By using the modified nonlinear travel time tomography method and combining the datasets from CNMSN and PANDA, Powell et al. [2010] imaged the 3-D  $V_p$ ,  $V_s$  and  $V_p/V_s$  models with a smaller horizontal grid size of  $2\text{ km} \times 2\text{ km}$  and good resolution to the depth of 8.65 km.  $V_p$ ,  $V_s$  and  $V_p/V_s$  models for the upper crust of the NMSZ were improved by Dunn et al. [2013] after using a different tomography approach (double-difference local earthquake tomography) and longer-period datasets from CNMSN and PANDA.

With the benefit of incorporating teleseismic events so that deeper structure information can be accessed, a lithospheric velocity model was built for the NMSZ [Zhang et al., 2009]. The tomographic inversion result of Zhang et al. [2009] revealed a low velocity zone in the lower crust and upper mantle within the Reelfoot rift, while the high-velocity mafic intrusions proposed in previous studies were not detected. The deep low velocity zone was considered to be a shear zone at rheological boundaries, which allows stress to be shifted from the weak zone in the deep layer up to the seismogenic faults in the upper crust. This hypothesis was able to explain the high intraplate seismicity in the NMSZ without a high strain rate indicated by GPS measurements [Newman et al., 1999; Calais et al., 2005; Calais and Stein, 2009]. Chen et al. [2014] proposed a 3-D P-wave velocity model revealing the lithospheric structure beneath the NMSZ down to 400 km depth with recent local events and teleseismic data collected by TA stations. Their  $40\text{ km} \times 40\text{ km}$  grid-size model supported the hypothesis of the weak zone under the NMSZ but in a deeper layer (50-200 km depth) and broader scale.

Although the traditional body wave travel time tomography method with earthquake data has provided the image of lithospheric velocity structure beneath the NMSZ, a uniform

resolution of the model is not likely to be achieved due to the infrequent and unevenly distributed events, and high-frequency signals are mostly lost in the teleseismic observations. To overcome these disadvantages above, the information carried in surface waves have been exploited and used for the inversion of more uniform- and higher-resolution velocity models.

With successful attempts of using ambient noise tomography (ANT) to generate high-resolution surface wave dispersion maps for California [Shapiro et al., 2005], western United States [Moschetti et al., 2007; Lin et al., 2008] and the whole North American continent [Bensen et al., 2008], Liang and Langston [2008] produced a Rayleigh wave group velocity model for the central and eastern North America with the northern embayment centered. The velocity maps were imaged from short period of 5 seconds to long period of 20 seconds, corresponding to the shallow upper crust and the whole crust structure, respectively. In their model, surface regional structures were imaged in the velocity maps obtained at the short periods, while the long period velocity maps revealed a strong correlation between the axial trend of ancient rift structures and the low velocity belts related to the deposited thick sediments. The overlap of the seismic zones with velocity transition area found in the model supported the reactivated Precambrian rift model in the NMSZ.

A 3-D shear wave velocity model can be created with surface wave velocity maps [Pollitz and Snoke, 2010; Mordret et al., 2014]. Pollitz and Mooney [2014] estimated a 3-D seismic shear wave velocity model of the central U.S. down to 240 km by analyzing long-period (18s - 125s) Rayleigh wave phase velocity maps. Their model demonstrated a weak mantle as evidenced by a low velocity zone extending down to at least 200 km depth under the Reelfoot rift. They hypothesized that the mantle weakness was caused by the compositional change during past magmatic events, and that the relatively thinner elastic plate resulted from the underlying low-viscosity mantle tended to concentrate tectonic stress near the strike-slip fault zone within the NMSZ.

With the capability of better resolving the vertical lithospheric heterogeneity, receiver function analysis approach was performed by Langston [1994] to study the crustal structure in the northern embayment. Constrained by previously published refraction data, a gradient crustal velocity model was proposed and the Moho boundary was estimated at about 40 km depth.

Joint inversion of surface wave dispersion and receiver functions has been conducted for the northern Basin and Range province [Ozalaybey et al., 1997] and Central and Western United States [Shen et al., 2013]. The good agreement between the inverted velocity model and the model constructed by other datasets or methods suggested the feasibility of this technique [Ozalaybey et al., 1997]. More detailed tectonic characteristics identified in the resulting shear velocity model indicated the improved resolution in the velocity model obtained from the joint inversion approach [Shen et al., 2013].

Although different methods have been carried out in the northern embayment for the purpose of investigating the crustal and mantle structure, joint inversion of surface wave dispersion and receiver functions, which, as mentioned above, has already exhibited its distinct strength, hasn't been performed yet.

## **2.1 The objective of this study**

In this research, we performed an ambient noise and receiver function analysis using newly available TA data to provide uniform coverage over the entire region, thus overcoming limitations of previous studies. These new datasets were used in a joint inversion for structure at each TA station as the first attempt to model velocity structure of the crust in 3-D.

## CHAPTER 3: METHODOLOGY

### 3.1 Surface wave analysis

#### 3.1.1 Rayleigh wave and Love wave

When an earthquake occurs and releases energy, seismic waves are generated and start to propagate through the Earth. Compared with body waves (including P- and S-waves), which transmit through the inner structure of the Earth, surface waves are the seismic waves that only travel along the outer layer. In a seismic record, surface waves can be easily recognized after the P- and S-wave arrivals for their low velocity, large amplitude and long duration. These characteristics are why surface wave observations play a significant role in seismology. So far, surface wave analysis has been used for the study of earthquake source inversion and the inversion of the lithospheric structure as in this research.

There are two types of surface waves based on their particle motions in the wavefront: Rayleigh wave and Love wave.

Rayleigh wave propagates along the free surface of a semi-infinite elastic half-space. As shown in Figure 10, its particle motion path is along a retrograde vertical ellipse, and the particle displacement decreases exponentially with increasing depth below the free surface. Since the particle motion of Rayleigh wave can be regarded as a combination of the P and SV waves, both the vertical and horizontal components of a seismometer are able to record the propagation of Rayleigh wave.

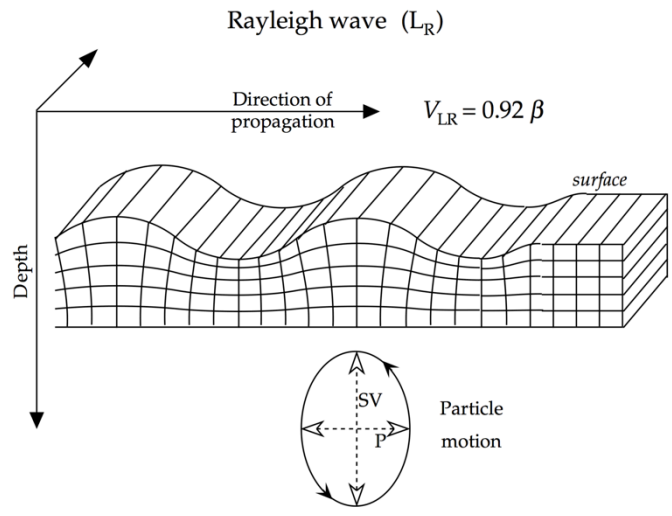


Figure 10: Particle motion of Rayleigh wave (Lowrie, 2007, pg. 136)

Love wave propagates within a horizontal layer between a free surface and a semi-infinite half-space when the S-wave velocity of the near-surface is lower than the velocity of the underlying half-space. The particles of Love wave move horizontally and perpendicular to the direction of wave propagation (SH-vibrations as shown in Figure 11), so Love wave propagation can only be recorded by horizontal component of seismometers.

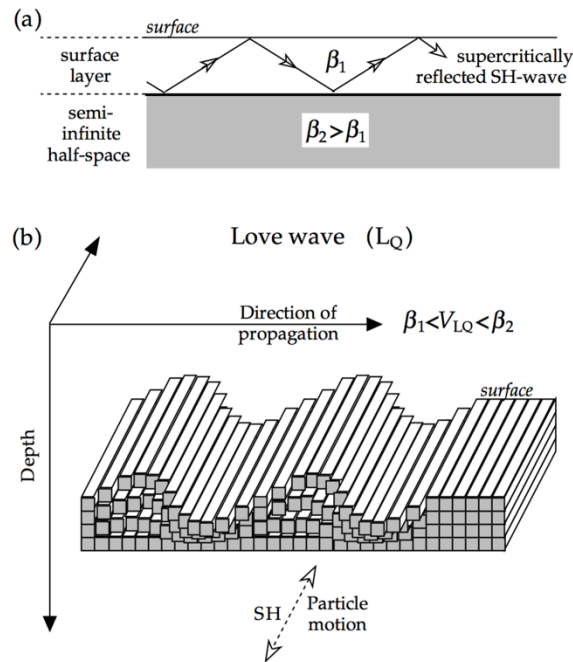


Figure 11: Particle motion of Love wave (Lowrie, 2007, pg. 137)

### 3.1.2 Dispersion

Surface waves, both Rayleigh and Love waves, have an important feature called dispersion. This refers to the phenomenon that the propagation speed of surface wave depends on the frequency.

For a uniform half-space with the Poisson's ratio of 0.25, the Rayleigh wave velocity equals to 0.92 of S-wave velocity and independent of frequency. The depth of penetration of the disturbance is proportional to period. For a more realistic velocity model, there is dispersion, but the shorter periods are controlled by shallow structure. Since short-wavelength (high-frequency) waves are more likely to be absorbed during propagation, long-wavelength (low-frequency) Rayleigh waves can propagate to larger distances deeply into the Earth. For Love wave, the dispersion is demonstrated by that the velocity of short-wavelength wave is close to the slower velocity of the near-surface while the velocity of long-wavelength wave approaches the faster velocity of the underlying half-space.

Since the dispersion of both Rayleigh and Love waves is related to the anisotropy of the medium, this feature can be used to study the lithospheric structure.

### 3.1.3 Phase velocity and Group velocity

When describing the propagating velocity of surface waves, two types of velocities are involved: phase velocity  $c$  and group velocity  $U$ . Phase velocity is defined as the velocity with which a particular phase (peak or trough) travels. Group velocity is the velocity with which surface wave energy associated with a particular frequency travels. They are determined by the relations:

$$c = \frac{\omega}{k},$$

$$U = \frac{d\omega}{dk} = c + k \frac{dc}{dk},$$

where  $\omega$  is angular frequency and  $k$  is wavenumber.

Figure 12 shows dispersive surface waves obtained at increasing distances from the source.

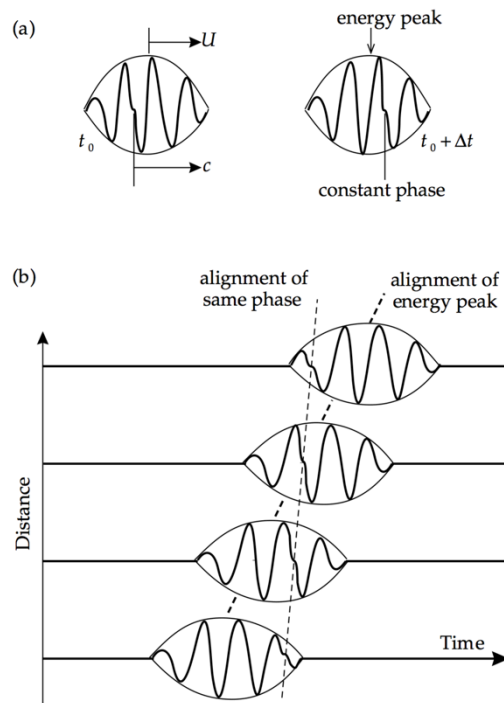


Figure 12: Dispersive surface waves at increasing distances and times (Lowrie, 2007, pg. 137)

Before we start to analyze the dispersion feature of surface waves, some mathematical background should be mentioned first.

### 3.1.4 Equations of motion for elastic medium

When an external body force is applied to an elastic medium, the medium will undergo a deformation, which means the particles of the medium are displaced from their original positions. The applied force per unit area is called stress, and the resulting deformation is called strain.

Based on Hooke's law for isotropic media, the relation between stress  $p_{ij}$  and strain  $e_{ij}$  is

$$p_{ij} = \lambda\theta\delta_{ij} + 2\mu e_{ij} .$$

In the formula, the Kronecker delta function  $\delta_{ij}$  is defined by

$$\delta_{ij} = \begin{cases} 1, & i = j \\ 0, & i \neq j \end{cases},$$

cubic dilatation  $\theta$  is the ratio of the change in volume to the original volume,

$$\theta = \frac{\partial u_x}{\partial x} + \frac{\partial u_y}{\partial y} + \frac{\partial u_z}{\partial z} = e_{xx} + e_{yy} + e_{zz},$$

strain  $e_{ij}$  is related to the displacement vector  $\mathbf{u} = (u_x, u_y, u_z)$ ,

$$e_{ij} = \frac{1}{2} \left( \frac{\partial u_i}{\partial x_j} + \frac{\partial u_j}{\partial x_i} \right),$$

and Lamé constants  $(\lambda, \mu)$  are determined by Young's modulus  $E = p_{xx}/e_{xx}$  and Poisson ratio  $\nu = -e_{zz}/e_{xx}$ :

$$\lambda = \frac{\nu E}{(1+\nu)(1-2\nu)},$$

$$\mu = \frac{E}{2(1+\nu)},$$

$\mu$  is also known as shear modulus or rigidity modulus, which is a measure of the resistance of the material to shearing strain

$$\mu = \frac{p_{ij}}{2e_{ij}}, \quad i \neq j.$$

As mentioned by Levshin (1973) and Aki and Richards (1980), the equations of motion for a point force acting inside a homogenous, isotropic elastic medium are given by

$$\rho \frac{\partial^2 u_x}{\partial t^2} = \frac{\partial}{\partial x} p_{xx} + \frac{\partial}{\partial y} p_{xy} + \frac{\partial}{\partial z} p_{xz} + f_x,$$

$$\rho \frac{\partial^2 u_y}{\partial t^2} = \frac{\partial}{\partial x} p_{xy} + \frac{\partial}{\partial y} p_{yy} + \frac{\partial}{\partial z} p_{yz} + f_y,$$

$$\rho \frac{\partial^2 u_z}{\partial t^2} = \frac{\partial}{\partial x} p_{xz} + \frac{\partial}{\partial y} p_{yz} + \frac{\partial}{\partial z} p_{zz} + f_z.$$

where  $u_i$  is the  $i$ th component of displacement vector  $\mathbf{u}$  and  $f_i$  is the  $i$ th component of body force per unit volume.

P-wave velocity  $\alpha$  and S-wave velocity  $\beta$  can be derived from these equations by Lamé constants  $(\lambda, \mu)$  and density  $\rho$  [Lowrie, 2007]:

$$\alpha = \sqrt{\frac{(\lambda+2\mu)}{\rho}},$$

$$\beta = \sqrt{\frac{\mu}{\rho}}.$$

### 3.1.5 Eigenfunction of surface waves

When we construct a half-space model with a top free surface in the Cartesian coordinate system, the solution to the motion equations is proven to be dominated by surface waves at large distances between source and observation site. The surface wave part of the solution can be separated into two independent fields with different polarizations: Rayleigh and Love waves. Assuming the solution to the equations of motion with no body force has the form of plane harmonic waves propagating along x-axis,

$$\mathbf{u}(\mathbf{x}, t) = \mathbf{V}(z)e^{i(\omega t - kx)},$$

where  $k$  is wavenumber,  $\omega$  is angular frequency,  $\mathbf{V}(z) = (V_x, V_y, V_z)$  is amplitude factor,  $(V_x, V_z)$  describes the velocity and amplitude of Rayleigh waves in the  $(x, z)$  plane and  $V_y$  describes the velocity and amplitude of Love waves along the y-axis. For simplicity, density  $\rho$  and shear modulus  $\mu$  are assumed to be constant at each layer.

For Love wave, the equation of motion can be written as

$$\frac{d}{dz} \left( \mu \frac{dV_y}{dz} \right) + (\rho\omega^2 - \mu k^2)V_y = 0,$$

or in matrix form,

$$\frac{d}{dz} \begin{bmatrix} V^{(y)} \\ p^{(yz)} \end{bmatrix} = \begin{bmatrix} 0 & 1/\mu \\ \mu k^2 - \rho\omega^2 & 0 \end{bmatrix} \begin{bmatrix} V^{(y)} \\ p^{(yz)} \end{bmatrix},$$

where the y component eigenfunction  $V^{(y)} = V_y$ ,  $p^{(yz)}$  is the amplitude factor for stress  $p_{yz}$ :

$$p_{yz} = p^{(yz)} e^{i(\omega t - kx)},$$

$k$  is the wavenumber,  $\omega$  is angular frequency,  $\mu$  is the rigidity and  $\rho$  is density.

When satisfying the boundary conditions that

- (a) at free surface  $z = 0$ , the stress  $p_{yz}$  is zero, or  $p^{(yz)} = 0$ ;
- (b) at the boundary  $z = H$ , the displacement  $V_y$  and stress  $p_{yz}$  are continuous;
- (c) as  $z \rightarrow \infty$ , the displacement  $V_y$  is finite and approaching to zero,
- the solution for a single layer over a half-space defines the dispersion relation:

$$\tan\left(kH\sqrt{\frac{c^2}{\beta_1^2}-1}\right) = \frac{\mu_2\sqrt{1-\frac{c^2}{\beta_2^2}}}{\mu_1\sqrt{\frac{c^2}{\beta_1^2}-1}},$$

where  $\mu_1, \mu_2$  and  $\beta_1, \beta_2$  are the rigidities and shear wave velocities of the layer between free surface and half-space (in the depth from 0 to H) and the half-space (in the depth deeper than H).

The dispersion feature of Love wave is well defined in this equation, and the phase velocity  $c$  can be determined when other parameters are given.

Another form of the solution satisfying the boundary conditions is

$$L = \omega^2 I_0 - k^2 I_1 - I_2,$$

where  $L$  is the Lagrangian, and

$$I_0 = \int_0^\infty \rho V^{(y)^2} dz,$$

$$I_1 = \int_0^\infty \mu V^{(y)^2} dz,$$

$$I_2 = \int_0^\infty \mu \left(\frac{dV^{(y)}}{dz}\right)^2 dz.$$

Thus, the Love wave group velocity  $U$  can be derived that

$$U = \frac{d\omega}{dk} = kI_1/\omega I_0.$$

For Rayleigh wave, the derived equation can be written in matrix

$$\frac{d}{dz} \begin{bmatrix} V^{(z)} \\ V^{(x)} \\ p^{(zz)} \\ p^{(xz)} \end{bmatrix} = \begin{bmatrix} 0 & k\lambda/(\lambda+2\mu) & 1/(\lambda+2\mu) & 0 \\ -k & 0 & 0 & 1/\mu \\ -\rho\omega^2 & 0 & 0 & k \\ 0 & -\rho\omega^2 + 4k^2\mu(\lambda+\mu)/(\lambda+2\mu) & -k\lambda/(\lambda+2\mu) & 0 \end{bmatrix} \begin{bmatrix} V^{(z)} \\ V^{(x)} \\ p^{(zz)} \\ p^{(xz)} \end{bmatrix},$$

where the  $x$  and  $z$  component eigenfunctions  $V^{(x)} = iV_x$ ,  $V^{(z)} = V_z$ ,  $p^{(zz)}$ ,  $p^{(xz)}$  are the amplitude factors for stresses  $p_{zz}$ ,  $p_{xz}$  :

$$p_{zz} = p^{(zz)} e^{i(\omega t - kx)} ,$$

$$p_{xz} = -ip^{(xz)} e^{i(\omega t - kx)} .$$

When satisfying the boundary conditions that

- (a) at free surface  $z = 0$ , the stresses ( $p_{xz}$ ,  $p_{zz}$ ) are zero, or  $p^{(zz)} = p^{(xz)} = 0$  ;
- (b) at the boundary  $z = H$ , the displacements ( $V_x$ ,  $V_z$ ) and stresses ( $p_{xz}$ ,  $p_{zz}$ ) are continuous;
- (c) as  $z \rightarrow \infty$ , the displacements ( $V_x$ ,  $V_z$ ) are finite and approaching to zero;

the solution is

$$L = \omega^2 I_0 - k^2 I_1 - 2k I_2 - I_3 ,$$

where  $L$  is the Lagrangian, and

$$I_0 = \int_0^\infty \rho [(V^{(z)})^2 + (V^{(x)})^2] dz ,$$

$$I_1 = \int_0^\infty [\mu (V^{(z)})^2 + (\lambda + 2\mu) (V^{(x)})^2] dz ,$$

$$I_2 = \int_0^\infty [\mu V^{(z)} \frac{dV^{(x)}}{dz} - \lambda V^{(x)} \frac{dV^{(z)}}{dz}] dz ,$$

$$I_3 = \int_0^\infty [(\lambda + 2\mu) \left(\frac{dV^{(z)}}{dz}\right)^2 + \mu \left(\frac{dV^{(x)}}{dz}\right)^2] dz .$$

So the Rayleigh wave group velocity  $U$  can be determined that

$$U = \frac{d\omega}{dk} = (kI_1 + I_2) / \omega I_0 .$$

### 3.2 Ambient Noise Tomography (ANT)

In this study, ambient noise tomography (ANT) was used to estimate Rayleigh/Love wave group/phase velocity maps in the northern embayment. The basic idea of ANT is that surface wave observations used for tomography are extracted from background ambient noise. Compared with teleseismic data, whose high frequency contents are usually missing due to

inherent scattering and attenuation, the surface wave measurements produced by recorded ambient noise are able to preserve high-frequency contents, which leads to a higher resolution at a shallow depth range. In addition, considering the randomized distribution of the ambient sources when averaged over a long time, the ANT can yield a better velocity model for both seismic and aseismic regions with homogenous resolution [Shapiro and Campillo, 2004; Shapiro et al., 2005; Moschetti et al., 2007].

The procedure for the approach of ANT is as follows: the Green functions of surface waves can be determined by cross correlating long-sequence ambient noise recorded at station pairs. After analyzing the obtained Green functions using the multiple filter analysis technique, surface wave dispersion curves can be estimated, showing the variation of group and phase velocities at different periods along different paths. By dividing the raypath length by group or phase velocity at a certain period, the travel times can be calculated and used to perform tomographic inversion to achieve Rayleigh/Love wave group/phase velocity maps at different periods with uniform lateral resolution in the study area [Bensen et al., 2007, 2008; Cho et al., 2007; Liang and Langston, 2008; Lin et al., 2008].

### **3.2.1 Multiple Filter Analysis (MFT)**

Surface wave spectrum is proven to be containing a lot of useful information. Based on this fact, the Multiple Filter Analysis technique is performed to analyze the spectrum of a multi-mode dispersed seismic signals and estimate the surface wave group velocities by Dziewonski et al. [1969] and Herrmann [1973]. The basic theory of this technique is that when the original dispersed signals are passed through a set of narrow-band Gaussian filters with different center frequencies, the maximum spectral amplitude of the filtered signals can be found and used to determine the group velocities [Herrmann, 2002].

Given a dispersed surface wave composed of  $M+1$  modes, the displacement of the signal at time  $t$  and distance  $r$  can be represented by the equation

$$f(t, r) = \frac{1}{2\pi} \int_{-\infty}^{\infty} F(\omega, r) \exp(i\omega t) d\omega = \frac{1}{2\pi} \int_{-\infty}^{\infty} \sum_{j=0}^M A_j(\omega, r) \exp [i(\omega t - k_j r) + \varphi] d\omega ,$$

where

$$F(\omega, r) = \sum_{j=0}^M A_j(\omega, r) \exp (-ik_j r + \varphi) ,$$

and  $\omega$  is the angular frequency,  $A_j$  is the  $j$ -th mode spectrum amplitude,  $k_j$  is the  $j$ -th mode wavenumber, and  $\varphi$  is the source phase.

For one applied Gaussian band-pass filter with a center frequency of  $\omega_0$  and cutoff frequencies of  $\omega_0 \pm \omega_c$ , the filtering function is defined as

$$H(\omega) = \begin{cases} \exp\left(-\frac{\alpha\omega^2}{\omega_0^2}\right) & |\omega| \leq \omega_c \\ 0 & |\omega| > \omega_c \end{cases} ,$$

where the filter parameter  $\alpha$  is related to the variance of the Gaussian curve and controls the resolution.

After applying the Gaussian filter to the dispersed signal, the complex filtered multi-mode time signal is approximately given by

$$g(t, r) = \frac{\omega_0}{2\pi} \sqrt{\frac{\pi}{\alpha}} \sum_{j=0}^M A_j(\omega_0, r) \exp [i(\omega_0 t - k_{0,j} r) + \varphi] \exp \left[ -\frac{\omega_0^2}{4\alpha} (t - r/U_{0,j})^2 \right] ,$$

where  $U_{0,j}$  is the group velocity of  $j$ -th mode surface wave at frequency  $\omega_0$  with the expression  $U_{0,j} = \frac{d\omega_0}{dk_j}$ , and  $k_{0,j}$  is the first term of the first-order Taylor series expansion of  $j$ -th mode wavenumber  $k_j(\omega)$  about  $\omega = \omega_0$ , e.g.

$$k_j(\omega) = k_{0,j} + \frac{dk_j}{d\omega_0} (\omega - \omega_0) + \frac{1}{2} \frac{d^2k_j}{d\omega_0^2} (\omega - \omega_0)^2 .$$

Because of the last exponential function term in  $g(t, r)$ , the maximum envelopes of the filtered signal are reached when  $t = r/U_{0,j}$ , which is the group velocity arrival. In this case, the group velocity can be estimated from the time of envelope maximum when the

spectral amplitude reaches its peak with the maximum envelope amplitude  $|g(t = -r/U_{0,j}, r)|$ , e.g.

$$A_j(\omega_0, r) = \frac{2\pi}{\omega_0} \sqrt{\frac{\alpha}{\pi}} |g(t = \frac{r}{U_{0,j}}, r)| ,$$

where

$$|g(t, r)| = \frac{\omega_0}{2\pi} \sqrt{\frac{\pi}{\alpha}} \sum_{j=0}^M A_j(\omega_0, r) \exp \left[ -\frac{\omega_0^2}{4\alpha} (t - r/U_{0,j})^2 \right] .$$

With the information of the group velocity arrival  $t = r/U_{0,j}$ , the phase expression of the filtered signal's spectrum is

$$\psi = \tan^{-1} \left[ \frac{\text{Im} g\left(\frac{r}{U_{0,j}}, r\right)}{\text{Re} g\left(\frac{r}{U_{0,j}}, r\right)} \right] = r\omega_0 \left( \frac{1}{U_{0,j}} - \frac{1}{c_{0,j}} \right) + \varphi + N2\pi ,$$

where  $c_{0,j}$  is the phase velocity of j-th mode surface wave at frequency  $\omega_0$ , and  $N2\pi$  is resulted from the periodicity of  $\tan^{-1}$  function.

From the above equation, the phase velocity can be estimated when the source phase  $\varphi$  is known.

Alternatively, Snieder [2004] and Wapenaar [2004] have shown how to estimate the source phase for the ambient noise empirical Green function. There is a slight modification to the phase velocity given by MFT. The unknown source phase  $\varphi$  can be eliminated when a two-station technique is used. If the two stations are deployed at the same azimuth from the source, the phase velocity can be calculated from the difference of their phase expression:

$$\psi_2 - \psi_1 = (r_2 - r_1)\omega_0 \left( \frac{1}{U_{0,j}} - \frac{1}{c_{0,j}} \right) + (N_2 - N_1)2\pi .$$

### 3.2.2 Least-square tomographic inversion

The least-square inversion is performed to obtain Rayleigh/Love wave group/phase velocity maps at different periods, or called velocity models, with uniform lateral resolution.

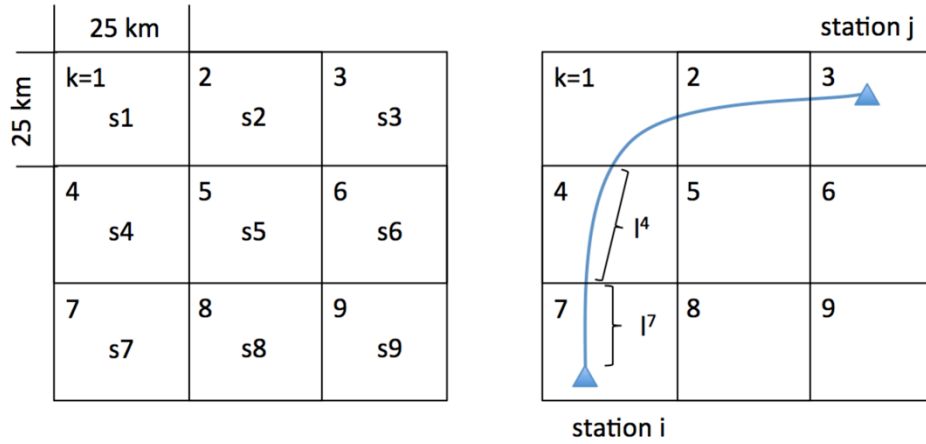


Figure 13: Least-square inversion grids

*Note.* Left: example of a velocity model with 9 cells;  $s$  represents the slowness (the reciprocal of velocity). Right: raypath across 5 cells (1,2,3,4,7) between stations  $i$  and  $j$ ; raypath length in each cell ( $k$ ) is indicated as  $l^k$ .

Velocity models can be constructed in the form of 2-D cells at different periods. In this study, the interest area has been divided into uniform cells with the size of  $25 \text{ km} \times 25 \text{ km}$ . An example is shown in Figure 13. When the cell size is determined, a starting model will be estimated by assigning values as slowness ( $s_k$ ) to each cell ( $k$ ), where the slowness ( $s_k$ ) is defined by the reciprocal of the velocity ( $1/v_k$ ). In other words, the model here can be seen as another means of the expression of velocity model. Assuming ray theory, we can measure the distances ( $l_k$ ) in the cells ( $k$ ) each ray goes between two stations ( $i, j$ ) and predict the travel time ( $t_{ij}$ ) by the equation:

$$t_{ij} = \sum_k l_k s_k .$$

If the raypath doesn't go through the cell  $k$ , the length  $l_k$  is 0.

In the matrix form, the equation is given by

$$d^{\text{pre}} = Gm ,$$

where  $d^{\text{pre}} = [t_{11}, t_{12}, \dots, t_{21}, t_{22}, \dots]^T$  denotes the predicted travel times ( $t_{ij}$ ) of surface waves (Rayleigh wave and Love wave) for a certain period between stations ( $i, j$ ) along great-

circle path,  $\mathbf{m} = [s_1, s_2, \dots]^T$  is a column vector including the slowness value ( $s_k$ ) of each cell ( $k$ ) at the same period, and the data kernel

$$\mathbf{G} = \begin{bmatrix} l_1^{11} & l_2^{11} & l_3^{11} & \dots \\ l_1^{12} & l_2^{12} & l_3^{12} & \dots \\ \dots & \dots & \dots & \dots \\ l_1^{21} & l_2^{21} & l_3^{21} & \dots \\ \dots & \dots & \dots & \dots \end{bmatrix}$$

contains the raypath length ( $l_k^{ij}$ ) across cells ( $k$ ) between station pairs ( $i, j$ ).

The observed travel times  $d^{\text{obs}}$  are calculated by dividing the raypath length by the group or phase velocity obtained from MFT.

To solve this linear inverse problem, the least square method is used to minimize the error between the observed travel times  $d^{\text{obs}}$  and the predicted travel times  $d^{\text{pre}}$  measured from a suggested model, e.g.

$$\text{MIN} = \|\mathbf{d}^{\text{obs}} - \mathbf{G}\mathbf{m}\|_2 .$$

Let the prediction error

$$\begin{aligned} E &= \mathbf{e}^T \mathbf{e} = (\mathbf{d}^{\text{obs}} - \mathbf{G}\mathbf{m})^T (\mathbf{d}^{\text{obs}} - \mathbf{G}\mathbf{m}) \\ &= \sum_{i=1}^N [d_i^{\text{obs}} - \sum_{j=1}^M G_{ij} m_j] [d_i^{\text{obs}} - \sum_{k=1}^M G_{ik} m_k] \\ &= \sum_{j=1}^M \sum_{k=1}^M m_j m_k \sum_{i=1}^N G_{ij} G_{ik} - 2 \sum_{j=1}^M m_j \sum_{i=1}^N G_{ij} d_i^{\text{obs}} + \sum_{i=1}^N d_i^{\text{obs}} d_i^{\text{obs}} , \end{aligned}$$

the derivatives of  $E$  with respect to model parameters  $m_q$  should be set to be zero, e.g.

$$\begin{aligned} \frac{\partial E}{\partial m_q} &= \sum_{j=1}^M \sum_{k=1}^M [\delta_{jq} m_k + m_j \delta_{kq}] \sum_{i=1}^N G_{ij} G_{ik} - 2 \sum_{j=1}^M \delta_{jq} \sum_{i=1}^N G_{ij} d_i^{\text{obs}} + 0 \\ &= 2 \sum_{k=1}^M m_k \sum_{i=1}^N G_{iq} G_{ik} - 2 \sum_{i=1}^N G_{iq} d_i^{\text{obs}} = 0 . \end{aligned}$$

In matrix notation, the equation can be written by

$$\mathbf{G}^T \mathbf{G} \mathbf{m} - \mathbf{G}^T \mathbf{d}^{\text{obs}} = 0 .$$

Presuming  $[\mathbf{G}^T \mathbf{G}]^{-1}$  exists, the estimated model parameters are

$$\mathbf{m}^{\text{est}} = [\mathbf{G}^T \mathbf{G}]^{-1} \mathbf{G}^T \mathbf{d}^{\text{obs}} .$$

When a priori info is added to the inverse problem that the solution is expected to be simple, the weighted combination of the solution length  $L$  and the prediction error  $E$  should be minimized, e.g.

$$\text{MIN} = E + \varepsilon^2 L = e^T e + \varepsilon^2 m^T m ,$$

where  $\varepsilon$  is the damping factor, and its value is chosen by trial and error.

The new solution is given by

$$m^{\text{est}} = [G^T G + \varepsilon^2 I]^{-1} G^T d^{\text{obs}} .$$

The inversion should be conducted iteratively with new modified model and repeatedly for different periods. In the end, the results can be combined together to build the final velocity model.

In tomographic inversion, a priori smoothness is incorporated to avoid abrupt horizontal velocity changes which are less likely to exist geologically.

### 3.3 Receiver function

Estimated from the teleseismic body waves recorded at 3-component seismic stations, receiver function is a time series (see Figure 15) after removing the source effect and the mantle propagation path effect from the observed waveform which only leaves the local near-receiver propagation path effect. Since the local path effect is a good indicator of discontinuities beneath seismic stations, receiver function has been developed to become a useful tool to image the crust and upper mantle structure [Langston, 1979; Ammon et al., 1990; Ammon, 1991, Herrmann and Ammon, 2002] and to define characteristic properties of the crust such as thickness and  $V_p/V_s$  ratio [Zhu and Kanamori, 2000].

Figure 14 shows an example of receiver function ray diagram with a plane-layered model. An incident teleseismic P wave is converted to S wave ( $P_s$ ) at the interface  $k$ . Multiples are generated between the free surface and the interface  $k$ . Because S waves travel

slower than P waves, the arrival time of Ps is longer than the direct P wave (Pp), and the arrival time difference can be calculated if the velocity model is given. This fact links the receiver function to the position of discontinuities in the lithospheric structure underneath the seismic station.

As shown in Figure 15, in the ideal case, receiver function will look like a spike train, a linear combination of impulses shifted in time. Those impulses correspond to the direct P wave and other converted phases marked in Figure 14. Since the receiver function traces are dominated by converted S waves, they are usually used to invert for shear wave velocity structure [Owens et al., 1984].

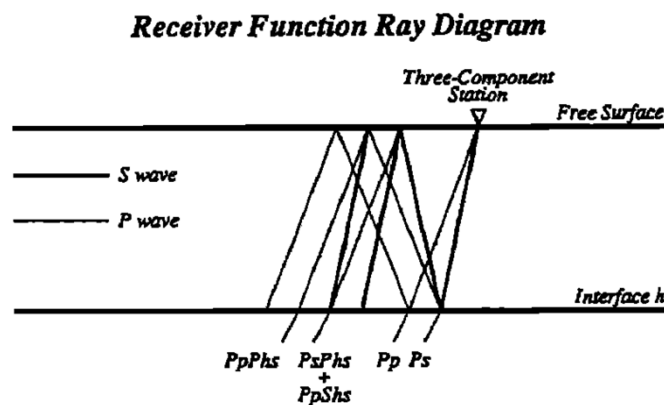


Figure 14: Receiver function ray diagram for a single layer over a half-space (Ammon et al., 1990, pg. 15304)

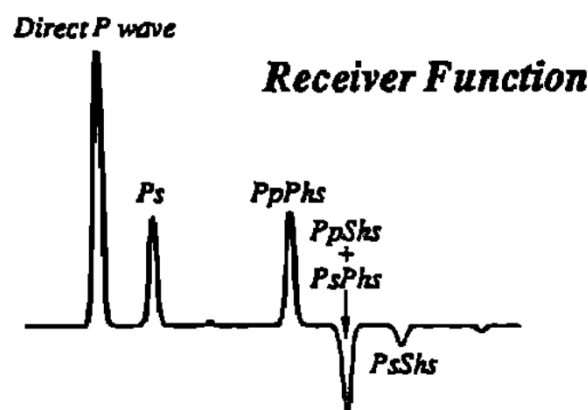


Figure 15: Receiver function trace (Ammon et al., 1990, pg. 15304)

In 1979, Langston proposed a source equalization technique to estimate the receiver function. He pointed out that the local path effect can be isolated by deconvolving the vertical component of a teleseismic P wave record from its horizontal components in the frequency domain. Ammon [1991] modified this technique and preserved the true amplitude of the receiver function, which further constrains the inversion of velocity structure. However, a problem for the frequency domain deconvolution is that the Fourier transform of the horizontal components of the seismogram needs to be calculated. In this study, the iterative time domain deconvolution approach is applied to estimate the receiver functions. This approach was developed by Kikuchi and Kanamori [1982] and implemented by Ligorría and Ammon [1999]. The program code used in this study, called `saciterd`, was written by Dr. Charles J. Ammon.

The first step of this approach is to calculate the cross-correlation between the observed vertical and horizontal component. The resulting optimal time is the lag of the first largest impulse in the receiver function. Since the amplitude of the impulse can be estimated easily, the lag and amplitude of the first impulse compose a temporary receiver function. The next step is to convolve the temporary receiver function with vertical component and subtract it from the horizontal component. The third step is to repeat the cross-correlation with the new horizontal signal and then add the estimated lag and amplitude of the second impulse to the temporary receiver function. Each time the receiver function is updated with another impulse, the subtraction result in the second step decreases. The second and third steps are repeated until the reduction in misfit with the updated receiver function is small enough.

### **3.4 Joint inversion**

Joint inversion of surface wave dispersion and teleseismic P-wave receiver functions is performed to construct a hybrid 1D-3D shear wave velocity model of the study area. Each

of these two datasets provides different advantages in lithospheric structure imaging. For surface wave dispersion, the velocity structure information above a certain depth is presented in an average sense, while for receiver functions, the sharp velocity contrasts in the shallow structure are targeted. In this case, the addition of receiver function to the surface wave inversion undoubtedly better constrains the vertical shear wave velocity variation. On the other hand, the relative arrival time difference is measured in the receiver function inversion, so a depth-velocity trade-off becomes an inevitable problem which leads to more than one possible resulting model [Ammon et al., 1990]. Joint interpretation of the two datasets can also reduce the chances of non-unique results the inversion with only one single dataset could bring.

The linear damped least-square approach used in this study has been attempted by Julia et al. [2000]. A weighting factor is incorporated to combine and evaluate the influence of each dataset. The prediction error that should be minimized in the sense of least squares is

$$S = \frac{(1-p)}{N_r} \sum_{i=0}^{N_r} \left( \frac{O_{r_i} - P_{r_i}}{\sigma_{r_i}} \right)^2 + \frac{p}{N_s} \sum_{j=0}^{N_s} \left( \frac{O_{s_j} - P_{s_j}}{\sigma_{r_j}} \right)^2 ,$$

where  $O_{xy}$ ,  $P_{xy}$ ,  $\sigma_{xy}$  indicate the observed data, predicted data and standard error at time  $t_y$ , the subscript r and s correspond to the receiver function dataset and surface wave dispersion dataset respectively, N is the total number of dataset observation, and p is the weighting factor which value is given between 0 and 1. Large p means more weight is put on the fitting of surface wave dispersion observations, while small p means more weight is put on fitting the observations of receiver functions [Herrmann and Ammon, 2002].

### 3.5 Model test

When the new hybrid 1D-3D shear wave velocity model is constructed, testing should be conducted to confirm the improvement made for the new model. With a well-determined source mechanism in the NMSZ, synthetic waveforms can be simulated by forward

computation using 1D velocity model beneath a certain station. If the velocity model is close to the real crustal and upper mantle structure, the synthetics should display similar features as the observed waveform recorded at the same station. If the constructed velocity model can't represent the actual subsurface structure, it's likely that distinct differences will be found between the synthetic and observed records. Notably, if the source mechanism is not well determined, for example the source depth is not accurate, the synthetic and observed waveforms may also demonstrate different characteristics even if the velocity model is correct.

Comparisons can also be made between different models. If the characteristics between the observed and synthetic waveforms show more consistency, the model used in forward computation is more favorable comparing to other models showing less consistent characters.

## CHAPTER 4: DATA

The ambient noise records used in this research were collected from over 100 3-component broadband stations of EarthScope Transportable Array (TA) from 2010 to 2014 (see Figure 16). These stations are operated by the Incorporated Research Institutions for Seismology (IRIS) and sponsored by the National Science Foundation (NSF). The TA stations used in this research span several states around the northern embayment, including Missouri, Illinois, Indiana, Kentucky, Arkansas, Tennessee, and northern Mississippi and Alabama. The interstation spacing is about 70 km.

Receiver function datasets were requested from IRIS. They were recorded from the same TA stations deployed in the northern embayment.

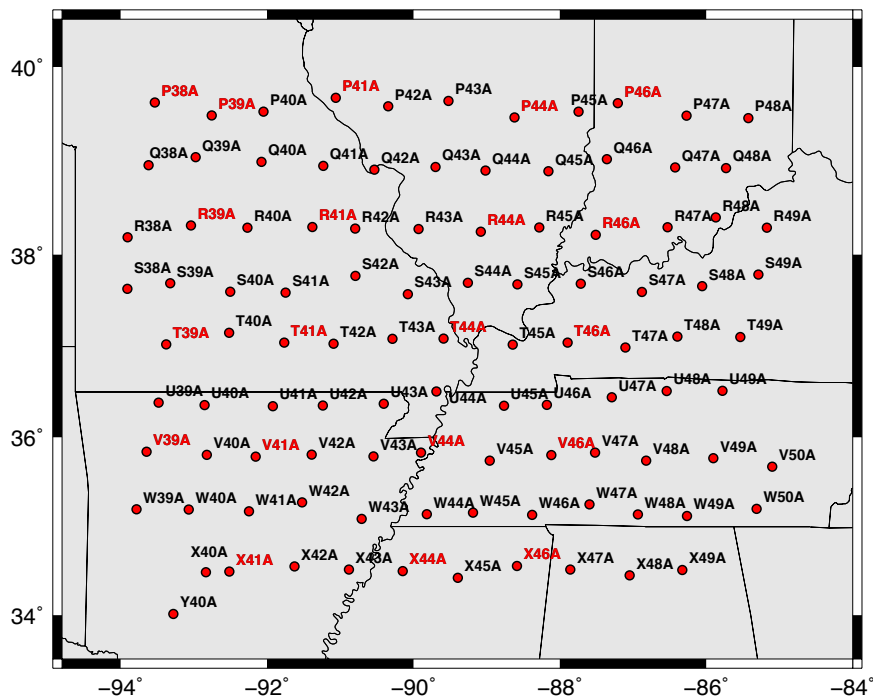


Figure 16: Distribution of TA stations around northern ME.  
*Note.* Stations listed in red are the master stations which were cross-correlated with all other stations.

Figure 16 shows the distribution of the TA stations deployed in the study area. To reduce the computational effort in creating the empirical Green's functions, we did not cross-correlate all stations. Instead, we selected a subset which was then cross-correlated with all other stations. The subset of "master" stations is indicated by the red-colored names. These stations were selected to provide a dense ray coverage.

## CHAPTER 5: RESULTS AND DISCUSSION

### 5.1 Dispersion maps

298671 points were picked in dispersion pattern in MFT and were used for surface wave tomography. During the inversion, the study area was divided into a uniform grid with the dimension of 25 km  $\times$  25 km. The inversion resulted in the Rayleigh/Love wave group/phase velocity models at periods of 2-50 seconds. The tomographic inversion program provided by Dr. Charles J. Ammon had smoothing in space and period, so that the dispersion curves at a grid node would be smooth.

#### 5.1.1 Checkerboard test

To test the raypath coverage and the reliability of the tomography program, we performed checkerboard tests before we inverted our real data.

Synthetic surface wave velocity models were constructed first. Assuming the same station distribution and ray paths, we calculated the traveltimes along the raypaths and created synthetic dispersion. Then we ran the inversion program with the synthetic data and obtained resulting models. The comparison between the inversion results and the synthetic models is able to tell the effectiveness of the inversion program and raypath coverage.

Figure 17 shows the synthetic surface wave group/phase velocity model. The high and low velocity perturbations are shown in blue and red symbols, where  $\pm 0.15$  km/s of 3 km/s are set to the fast and slow velocities in the checkerboard. Most high/low velocity blocks are made up of  $8 \times 8 = 64$  grid points except for the top and right ones. Since the study region for the model is bounded by 32-42N 81-96W, those top and right velocity blocks are cut in half by the boundaries of the study region.

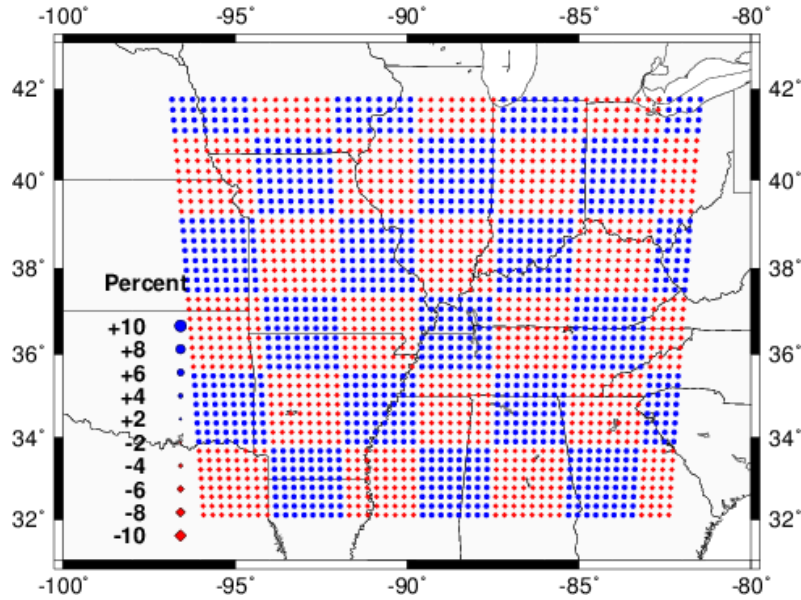


Figure 17: Synthetic surface wave velocity model

The checkerboard test results showed a good resolution at periods from 2 to 50 seconds. This means with the station distribution, raypath coverage and the inversion program we had, we should be able to obtain reasonable dispersion maps within certain geographical and period ranges. In addition, the information we got from the comparison between the resulting and synthetic model can also be used to obtain a more accurate interpretation of the real-data velocity models.

Figure 18 and Figure 19 show the test results at four selected periods for Love and Rayleigh phase velocities, respectively.

Figure 18 includes four Love wave phase velocity dispersion maps at periods of 3, 6, 12 and 24 seconds. The green rectangles on the maps mark the resolved region after comparing the resulting models to the synthetic models. The orange rectangles indicate the scope of the study area in Figure 3. Fast and slow velocity perturbations are also shown in blue and red symbols, and larger symbols correspond to larger differences between the local velocity and the average velocity shown on the right.

Some related information is listed to the right of each map. For example, in Figure 18 (a): at a short period of 3 seconds, the average velocity for the resulting model is 2.9955 km/s, with the maximum velocity of 3.197 km/s and the minimum of 2.836 km/s. 721 ray paths are used in tomography at this period.

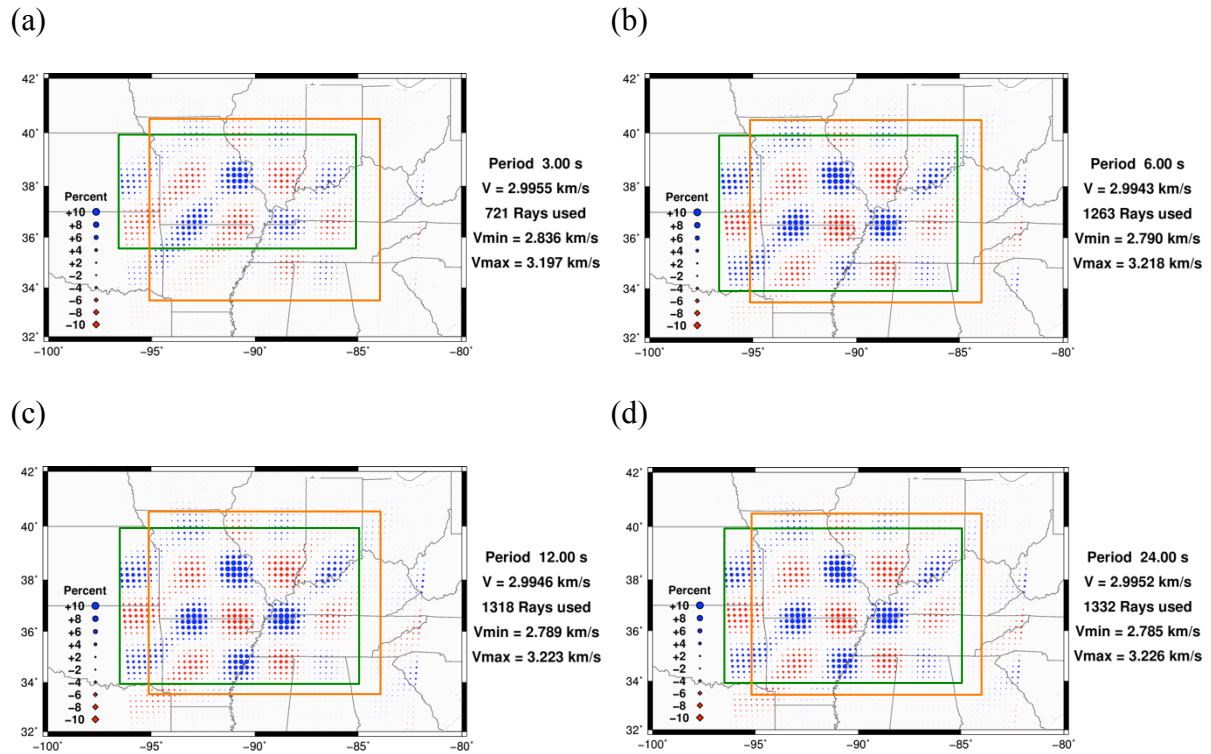


Figure 18: Checkerboard test for Love wave phase velocity dispersion maps at 3, 6, 12, 24 s

From the four dispersion maps, all the resulting dispersion maps show the checkerboard pattern as the synthetic model. Especially around the northern embayment, the velocity blocks are easily identified. The average velocities of the four maps are all close to the preset value of 3km/s even for the short period, but note that all average velocities are a little smaller.

With the marked green rectangles, we are able to determine which part of the dispersion maps to believe when calculating with real collected data. From Figure 17, the green resolved region at short period of 3 seconds has the range of 35.5-40N 85-97W. But at longer periods of 6, 12 and 24 seconds, the resolved regions are extended in the north-south

direction with the wider range of 34-40N, 85-97W. This is because dispersion curves are easier to identify at longer periods in MFT, thus more ray paths are included to constrain the velocity model during inversion process. Although the different sizes of the resolved region at short and long periods, all green rectangles are able to enclose the northern embayment where we are interested, so that the resolution of the results are sufficient for us to explore the ambiguous structural information of the study area in this research.

Figure 19 presents four Rayleigh wave phase velocity dispersion maps at periods of 3, 6, 12 and 24 seconds. These maps also display a good checkerboard pattern. The resolved regions have the same coordinate range, and the features shown from the maps are similar to the Love wave maps.

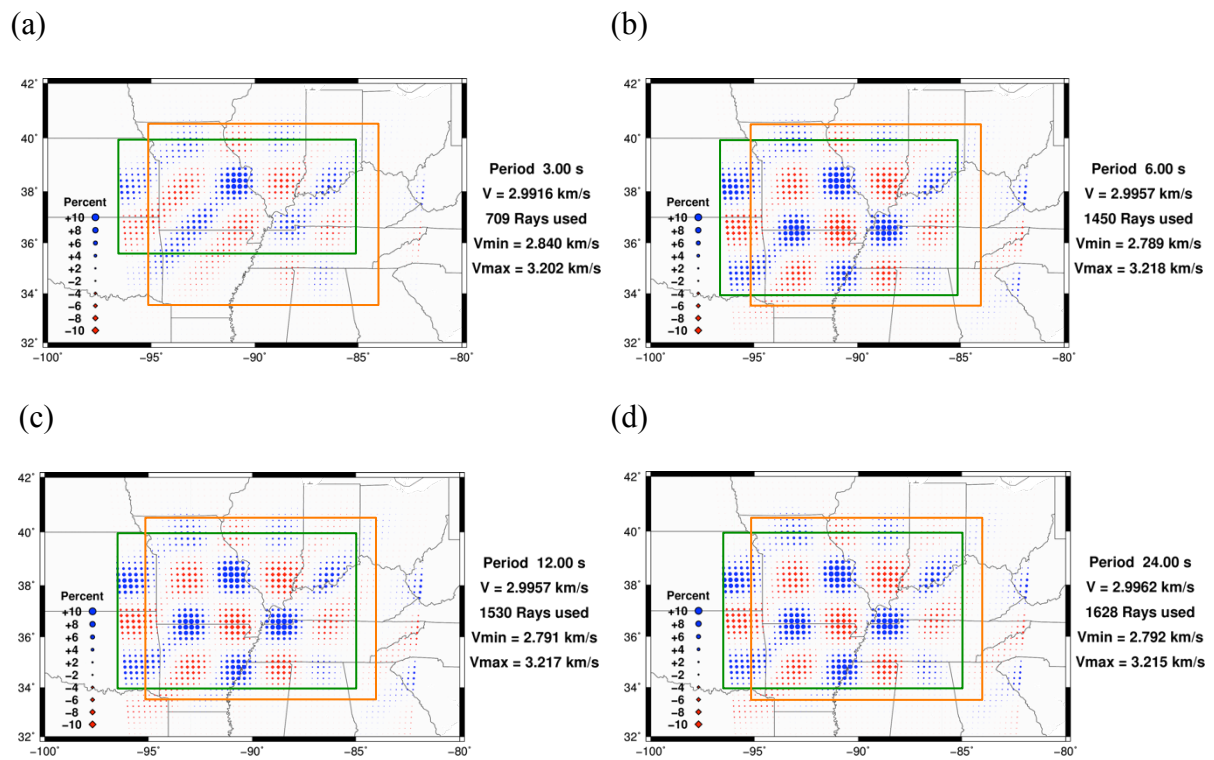


Figure 19: Checkerboard test for Rayleigh wave phase velocity dispersion maps at 3, 6, 12, 24 s

### 5.1.2 Real data result

Figure 20 and Figure 21 show the real-data Love/Rayleigh wave phase velocity dispersion maps at 3, 6, 12, 24 seconds. The green rectangles indicate the resolved region as in Figure 18 and Figure 19, and the orange rectangles show the study area in Figure 3.

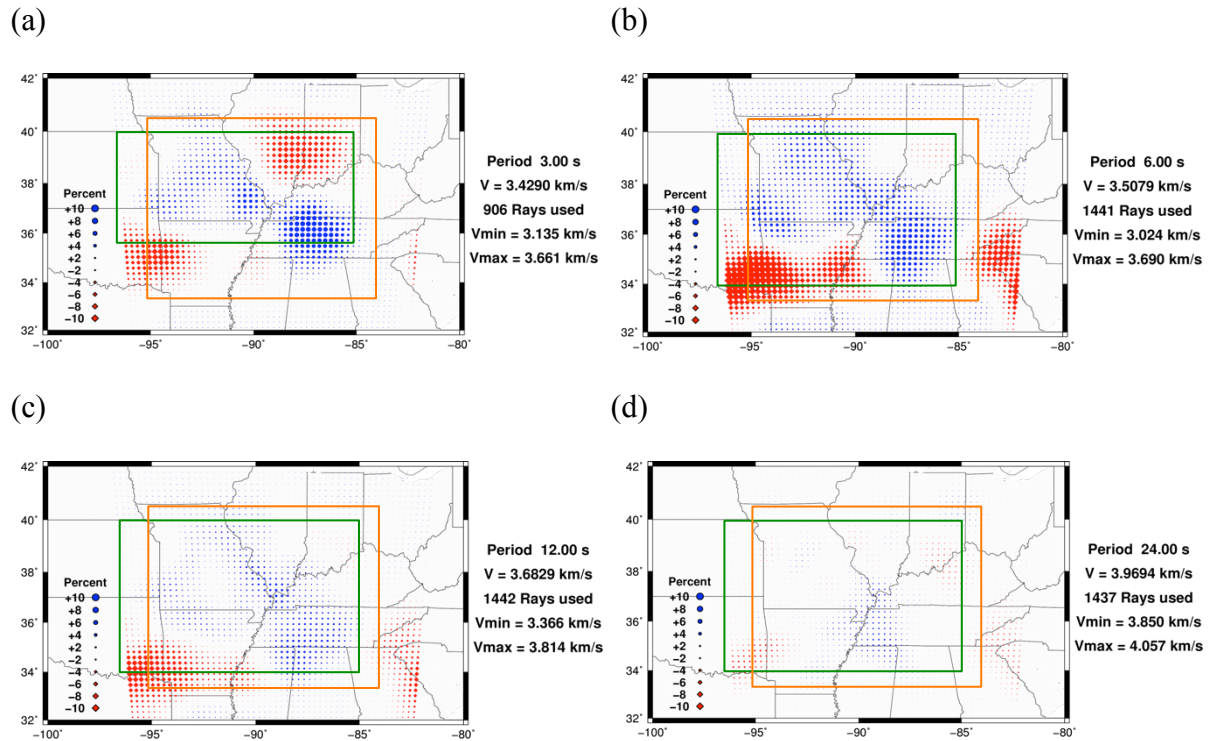


Figure 20: Love wave phase velocity dispersion maps at 3, 6, 12, 24 s

In the short-period dispersion map (Figure 20 (a)), the tectonic features like the Illinois basin (red low velocity anomaly) in the NE, the Ozark uplift (blue high velocity anomaly) in the west and the Nashville Dome (blue high velocity anomaly) in the east can be seen. At longer periods (Figure 20 (b,c,d)), the resolved region is enlarged and we start to see the low velocity anomaly in the SW. This low velocity anomaly is related to the Arkoma basin and the Ouachita Mountains which are composed of sedimentary rocks instead of the high velocity Paleozoic bedrocks. At the periods of 12 and 24 seconds (Figure 20 (c,d)), the strong velocity perturbations start to disappear, and this is because the structure at this depth tends to be the uniform Paleozoic bedrocks.

The Rayleigh wave dispersion maps shown in Figure 21 share the similar characteristics.

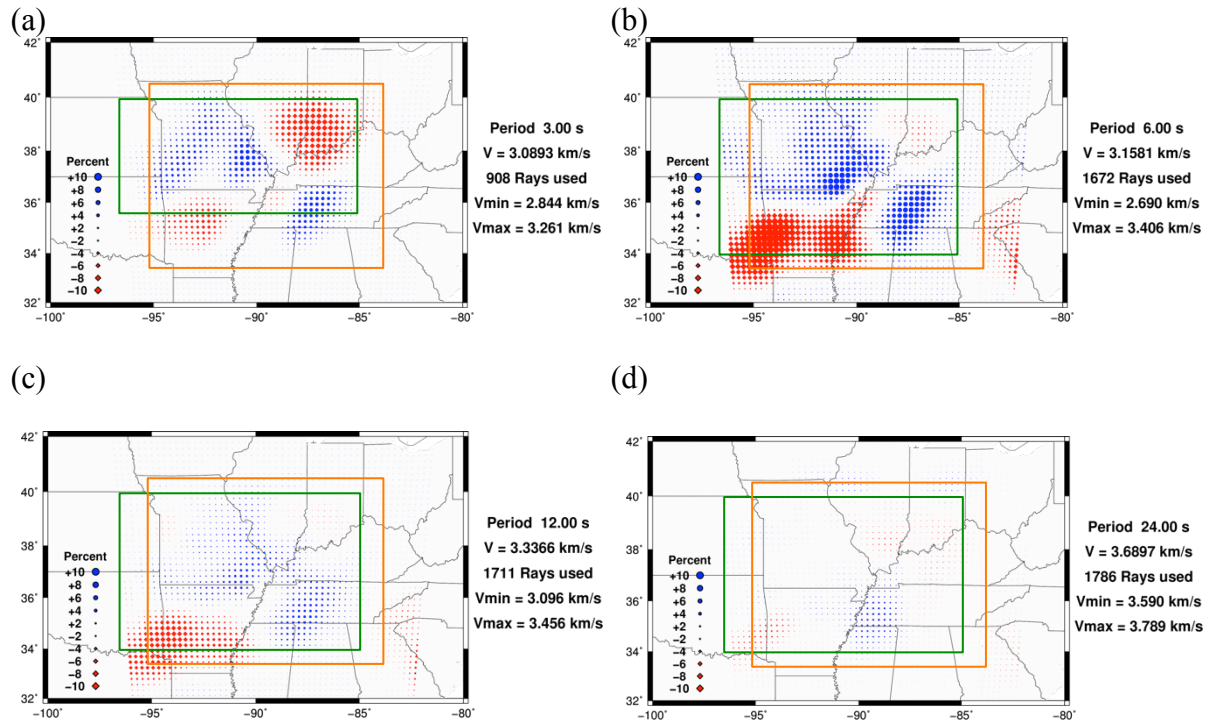


Figure 21: Rayleigh wave phase velocity dispersion maps at 3, 6, 12, 24 s

The fact that the features shown from the dispersion maps match the geological setting indicates the effectiveness of the collected data and the resulting dispersion maps and the method of surface wave tomography we adopted.

### 5.1.3 Dispersion curves comparison

With our constructed phase/group velocity models, surface wave dispersion was plotted showing the velocity variation with period at a specific location. Other researchers have also measured surface wave dispersion with different approaches and resolution in this area. To further analyze our results, our dispersion curves were plotted together with the dispersion obtained by other studies.

After comparison, we find most of our dispersion curves display a similar shape with others for the intermediate periods (8-50s), especially for phase velocity dispersion. Some

dispersion curves from other studies add more long period information (50-125s) which our study didn't focus on, but our dispersion contains more short period information (2-5s). A common phenomenon for all studies is that the phase velocity dispersion shows less scatter than group velocity dispersion for both Love and Rayleigh waves. Differences are also found in the dispersion shape between different studies.

Figure 22 and Figure 23 are two examples of the dispersion comparison, each of which has four dispersion plots: (a) Love wave phase velocity dispersion, (b) Rayleigh wave phase velocity dispersion, (c) Love wave group velocity dispersion, (d) Rayleigh wave group velocity dispersion. Dispersion curves measured from different researchers are marked in different colors.

As labeled in the right of the Figure 22 (a) and Figure 23 (a), our results in the period of 2-50 seconds are shown in light blue dots (NELE); yellow dots (EK13) are calculated from the phase-velocity model USANT13 obtained by Dr. Ekstrom in the period range of 5-40 seconds [Ekstrom et al., 1997; Larson and Ekstrom, 2001]; green dots (HRV) are from the research performed by Harvard Seismology Group for the longer periods of 32-150 seconds [Ekstrom, 2014]; red dots (NA) are from the surface wave tomography study for the whole North America performed by Dr. Herrmann using earthquake data; blue dots (OK) are obtained by Hao Guo for the Oklahoma area using joint inversion method; white dots (ASW) are estimated by the Automated Surface-Wave Phase-Velocity Measuring System (ASWMS) [Jin G. and J. B. Gaherty, 2015]; the blue (CUS) and red (WUS) curves are estimated from the faster central U.S. model [Herrmann, 1979] and slower western U.S. model [Herrmann et al., 2011]. Since both locations of these dispersion plots are near the New Madrid Seismic Zone in the central U.S., the estimated dispersion curves are closer to the blue CUS curves.

The coordinate position of the dispersion plots in Figure 23 is (36N, 91W), which is located near the west edge of the NMSZ. For the phase velocity dispersion, our results are

mostly overlain by others. But as the Figure 23 (a,b) shows, our dispersion curves have a smaller estimate of phase velocities than the EK13 results at the period range of 5-8 seconds. For the group velocity dispersion, the curves are less smooth than the phase velocity dispersion curves, and the differences between the curves from different studies are more obvious. Especially for Rayleigh wave group velocity dispersion, our dispersion curve indicates a lower velocity at short periods of 2-8 seconds than the red curve (NA).

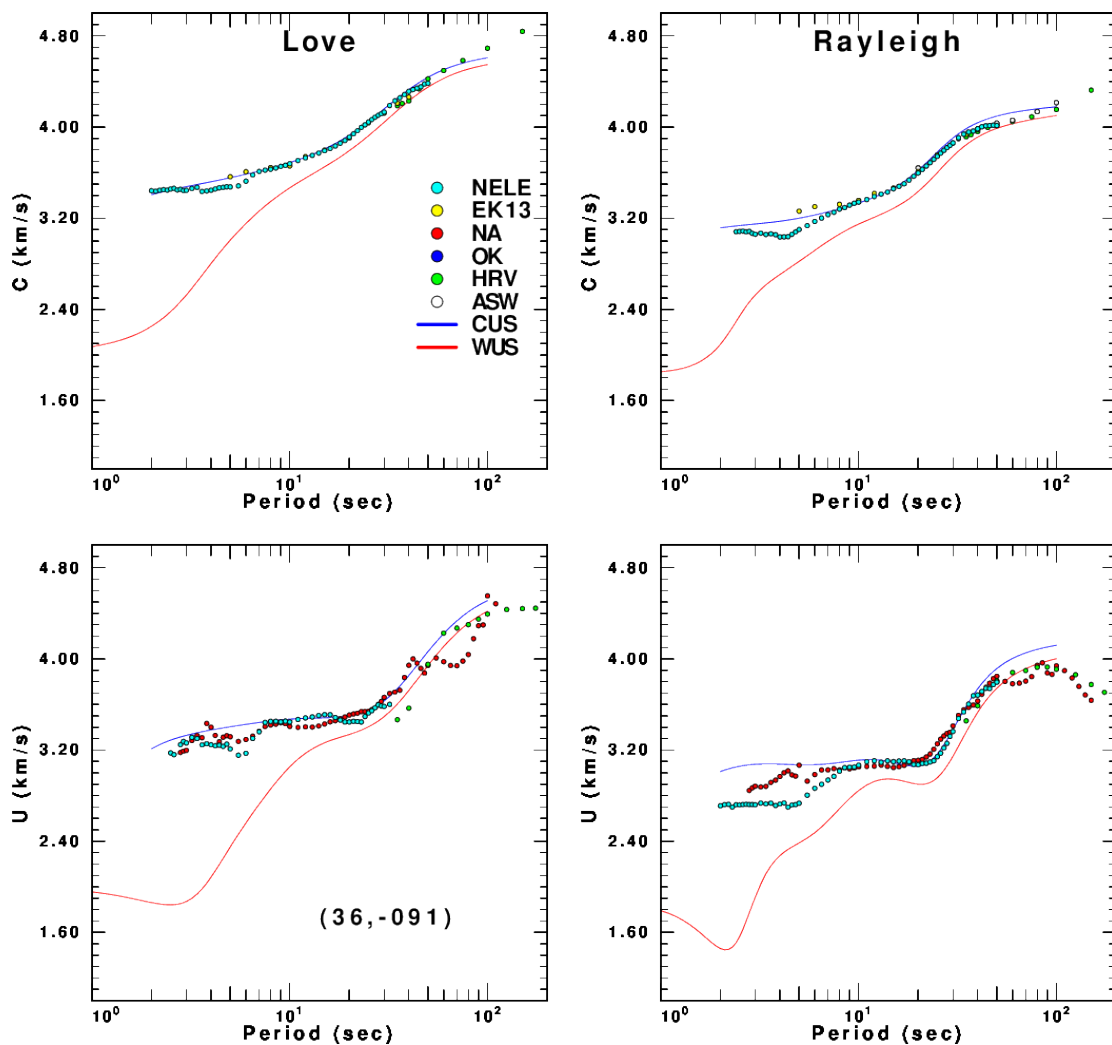


Figure 22: Comparison of Love/Rayleigh phase/group dispersion at (36N, 91W)

Compared with the other results, we believe our results (NELE) are more reliable. This is because our tomography is performed at local area with a narrower grid of 25 km,

while other results are obtained by regional or global tomography with a lower resolution. For example, the tomographic grid of the NA inversion model is 100 km. In addition, this short-period low velocity anomaly (compared with other studies) is observed on both our Rayleigh phase and group velocity dispersion.

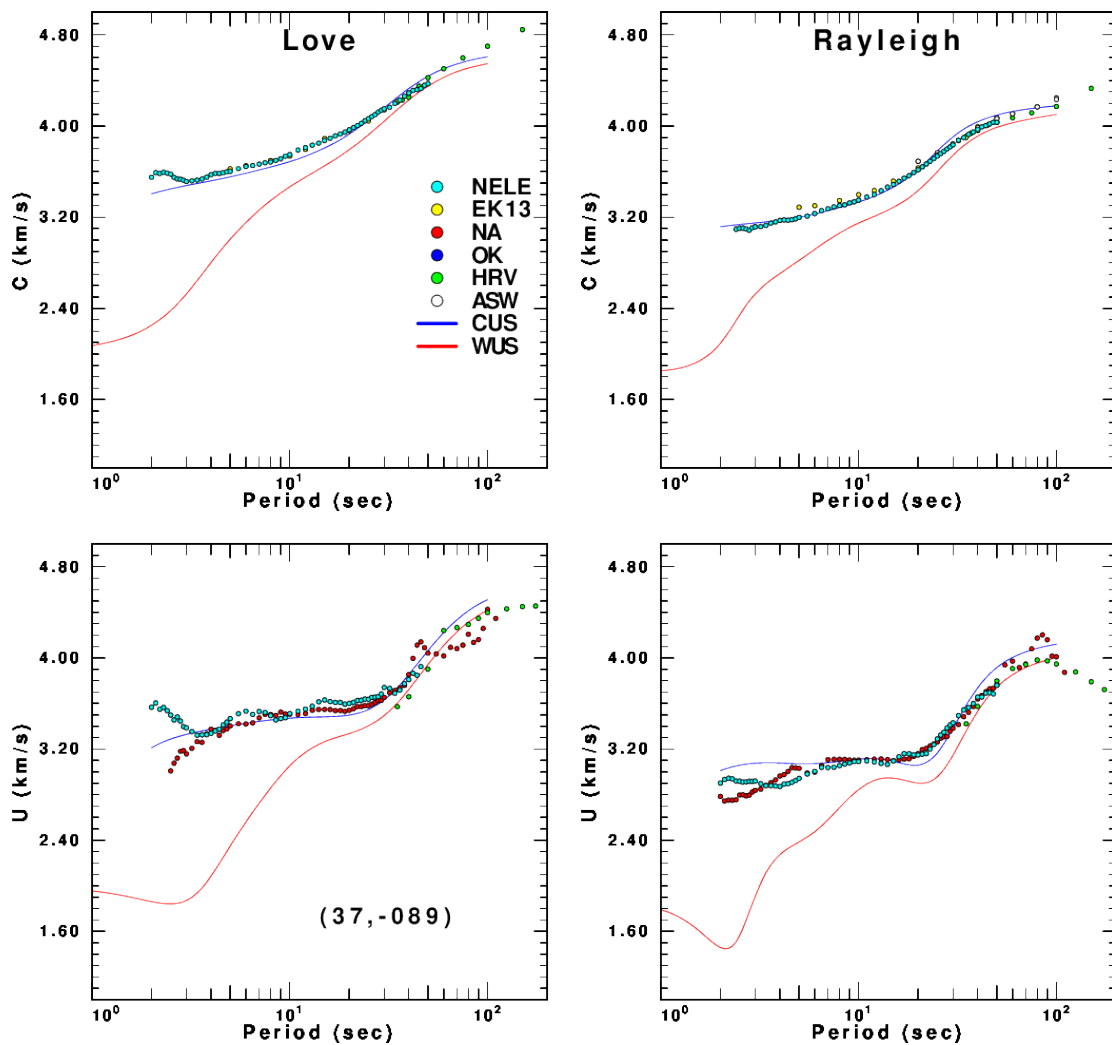


Figure 23: Comparison of Love/Rayleigh phase/group dispersion at (37N, 89W)

The dispersion plots in Figure 22 is at (37N, 89W), near the northern edge of the NMSZ. Our phase dispersion have a nice shape across the period of 2-50 seconds, except for a small unreasonable bump appearing at the period of 2-3 seconds in the Love wave dispersion. The short period information might be contaminated by the poor data quality

during processing. For the group velocity dispersion, NA curves and our results show a few differences at periods of 2-6 seconds.

In the Love wave group velocity dispersion plot, the shape of NA curve seems more rational than NELE, but for the Rayleigh wave, it's a little hard to decide which one is more reliable. Here I prefer the NELE curve because of the higher resolution I mentioned before, even though the NA curve has a more reasonable shape. More data added or other studies may provide more evidences of the right dispersion curve at this location.

We have also noticed that there is often a problem at periods less than 3 seconds, which may be due to the ability to pick dispersion short periods from ambient noise data.

## **5.2 1D Velocity maps**

With the tomographic results of dispersion and the receiver functions obtained from teleseismic P-wave records, we performed joint inversion and built 1D shear wave velocity models under each station. We started with the AK135 velocity model [Kennett et al., 1995] and then iteratively perturbed the model in a smooth manner to fit the dispersion and receiver functions.

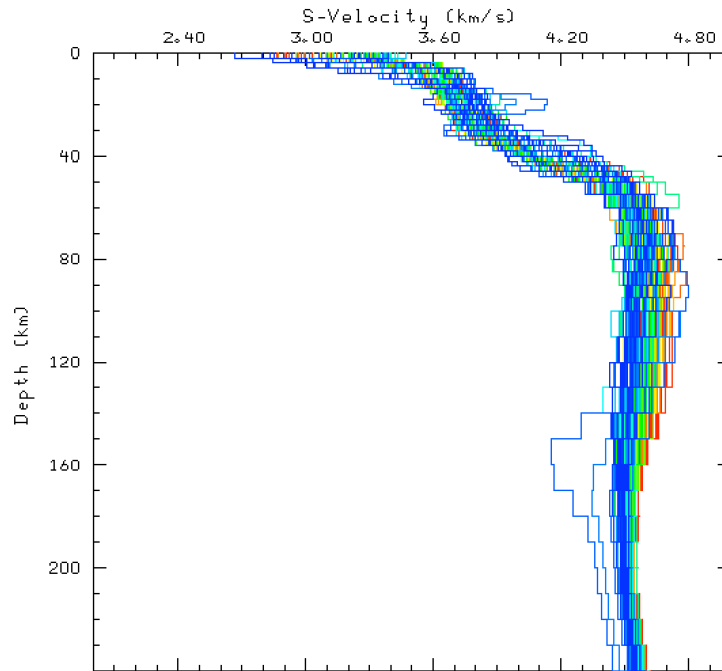


Figure 24: 1D shear wave velocity models at depth of 0-240km

Figure 24 shows all the S-velocity models to the depth of 240 km. In this Figure, all the velocity models we've obtained are stacked in one plot. The red velocity curves correspond to the stations located near the north side of the study area, and the blue ones are the stations near the south.

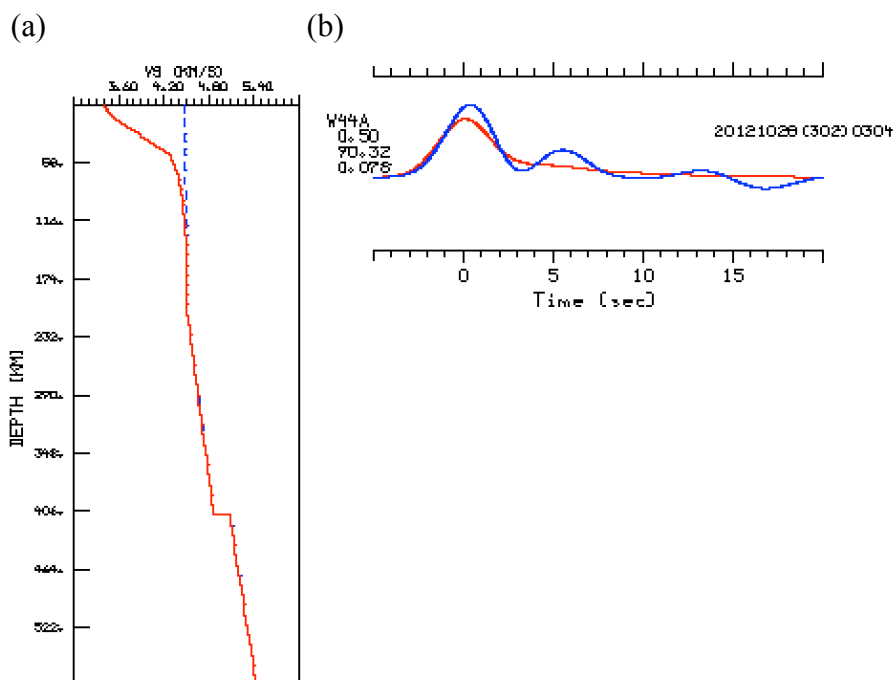
These S-velocity models display a similar behavior in a general way: the velocity starts at about 2.7-3.5 km/s at the near surface and gradually increases for the top 12 km. The velocity of the lower crust seems uniform, followed by a rapid increase between 35-50 km. However, the smooth trend between the depth of 60-80km is unexpected since it's often assumed that the Moho boundary should correspond to an abrupt velocity increase in most cases. The Moho is gradient like must reflect the long geologic history of the crust here.

From the distribution of the velocity curves in different colors, we can also find that the red ones have a higher velocity than the blue ones at the depth deeper than 80 km. This means the S-velocities under the northern stations are faster than the southern stations at the

same depth below the Moho boundary, which is expected from the dipping feature of the sediments-filled embayment.

Although most 1-D velocity models have a consistent behavior as shown in Figure 24, a specific velocity model can be easily identified with a much higher velocity of 4.15 km/s at 25 km depth and a much lower velocity of 4.15 km/s at 160 km depth. This deformed velocity model is under station W44A, and the reason for the less constrained model is the poor data quality.

Figure 25 and Figure 26 show the dataset and inversion results of the joint inversion of station W44A. The red curves in Figure 25 (a) and Figure 26 (a) are the initial model AK135 and the final model W44A, respectively. The observed receiver functions are shown in blue in Figure 25 (b) and Figure 26 (b). The black points in Figure 25 (c, d) and Figure 26 (c, d) are the observed dispersion from previous surface wave tomography and other studies. The predicted Love/Rayleigh wave dispersion and receiver functions with the initial and final models are indicated in red in Figure 25 (b, c, d) and Figure 26 (b, c, d).



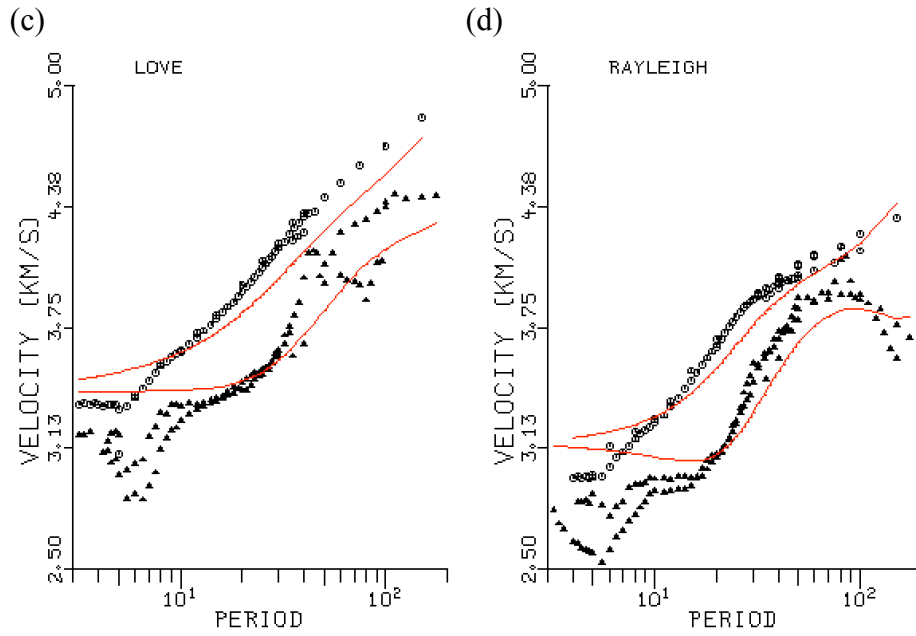


Figure 25: Velocity model and dataset before joint inversion under station W44A

- (a) initial model (b) receiver function dataset (c) Love wave phase/group velocity dispersion  
 (d) Rayleigh wave phase/group velocity dispersion

Since there is only one receiver function included in the joint inversion, the shallow structure can't be well constrained by the limited receiver function dataset. As for the surface wave measurements (Figure 26 (c, d)), only the Love wave phase dispersion shows a good match between the prediction and observation, and other dispersion curves are not well overlapped especially for the periods shorter than 10 seconds and between 40-100 seconds. These two mismatches could be related to the model deformation at depth of 25 km and 160 km.

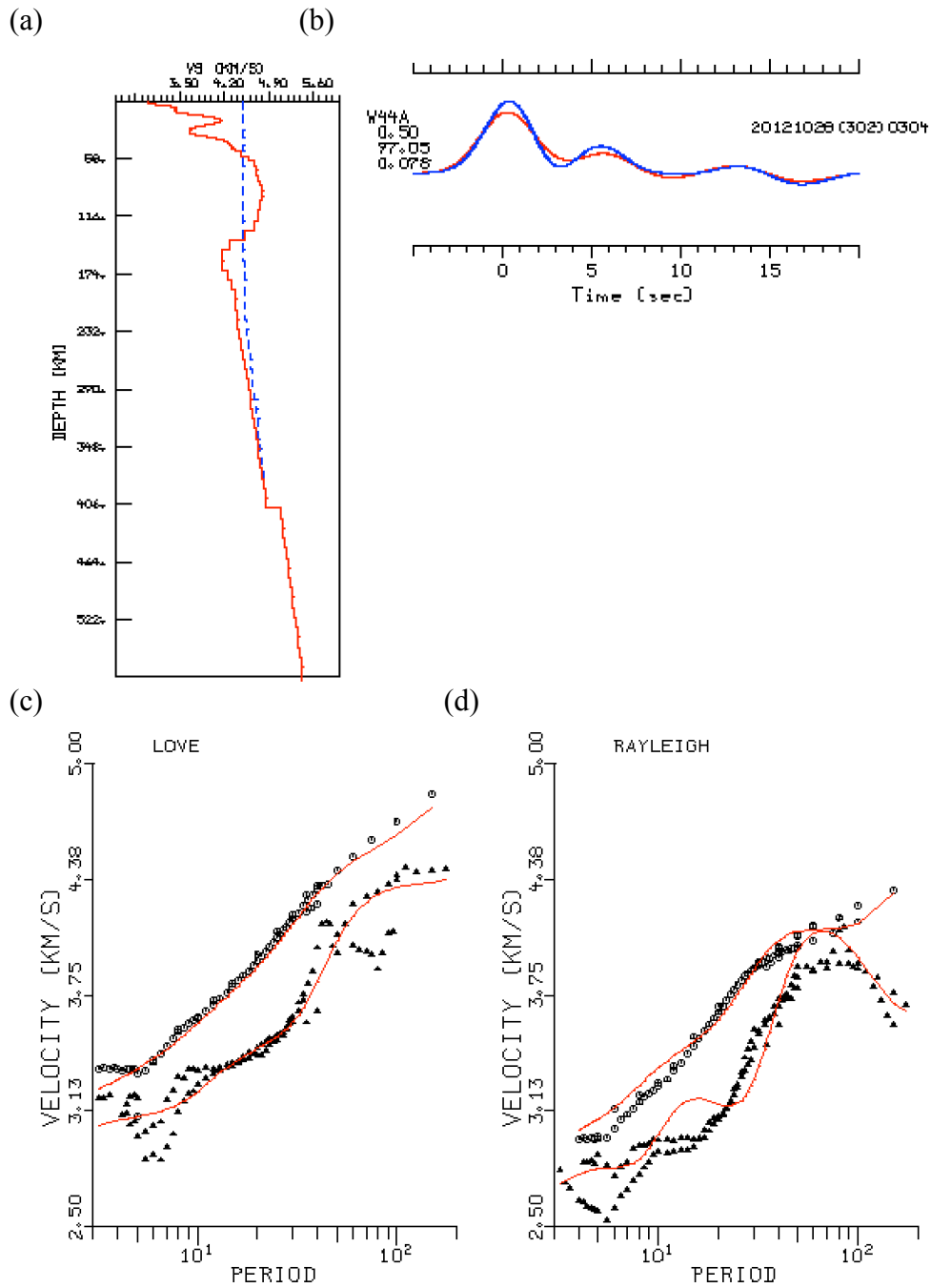
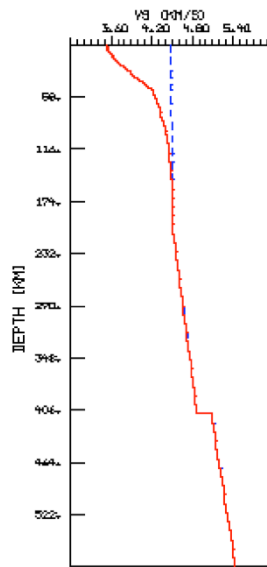


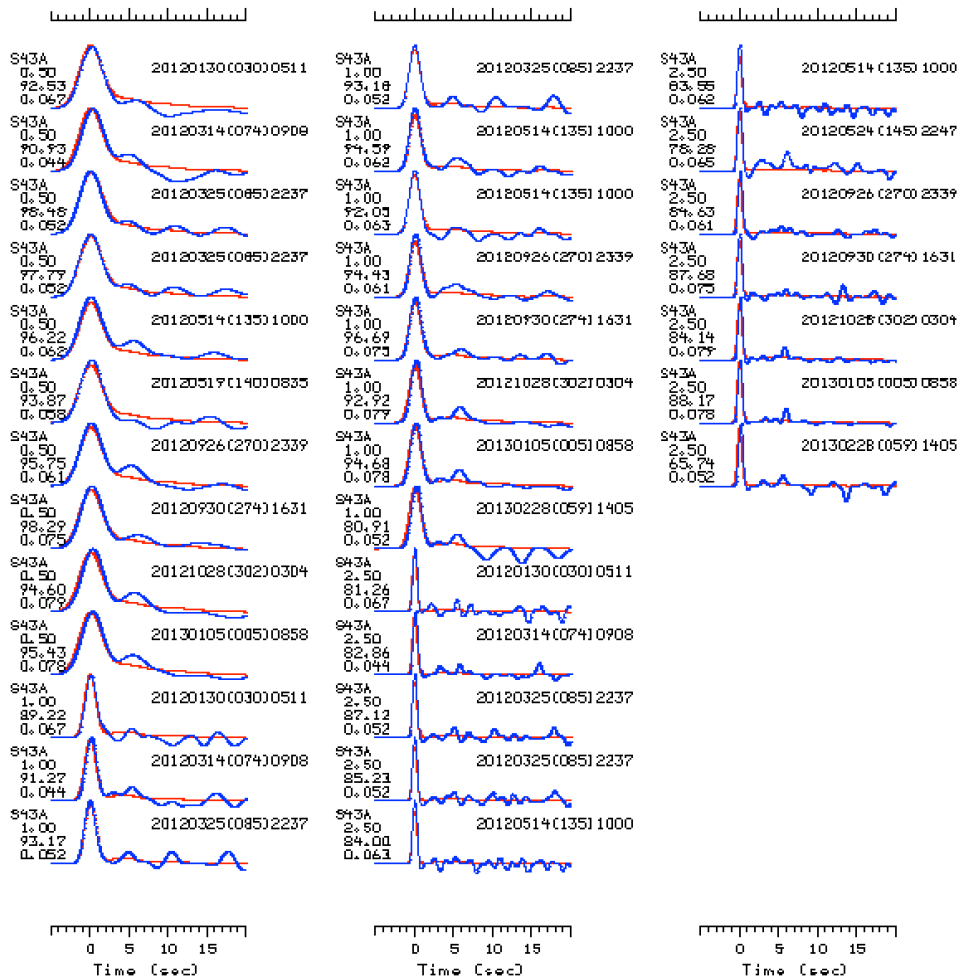
Figure 26: Velocity model and dataset after joint inversion under station W44A  
 (a) initial model (b) receiver function dataset (c) Love wave phase/group velocity dispersion  
 (d) Rayleigh wave phase/group velocity dispersion

As comparison, Figure 27 and 28 are the dataset and inversion results of station S43A.

(a)



(b)



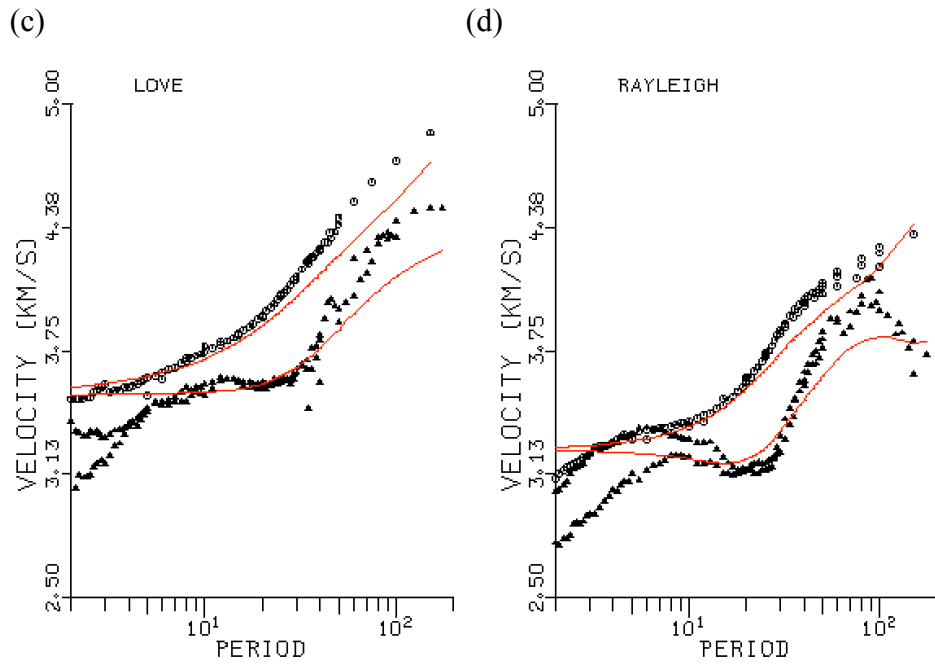
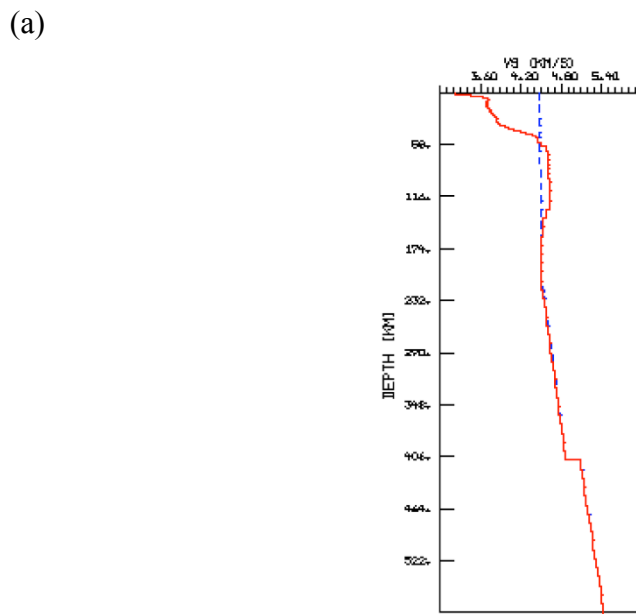
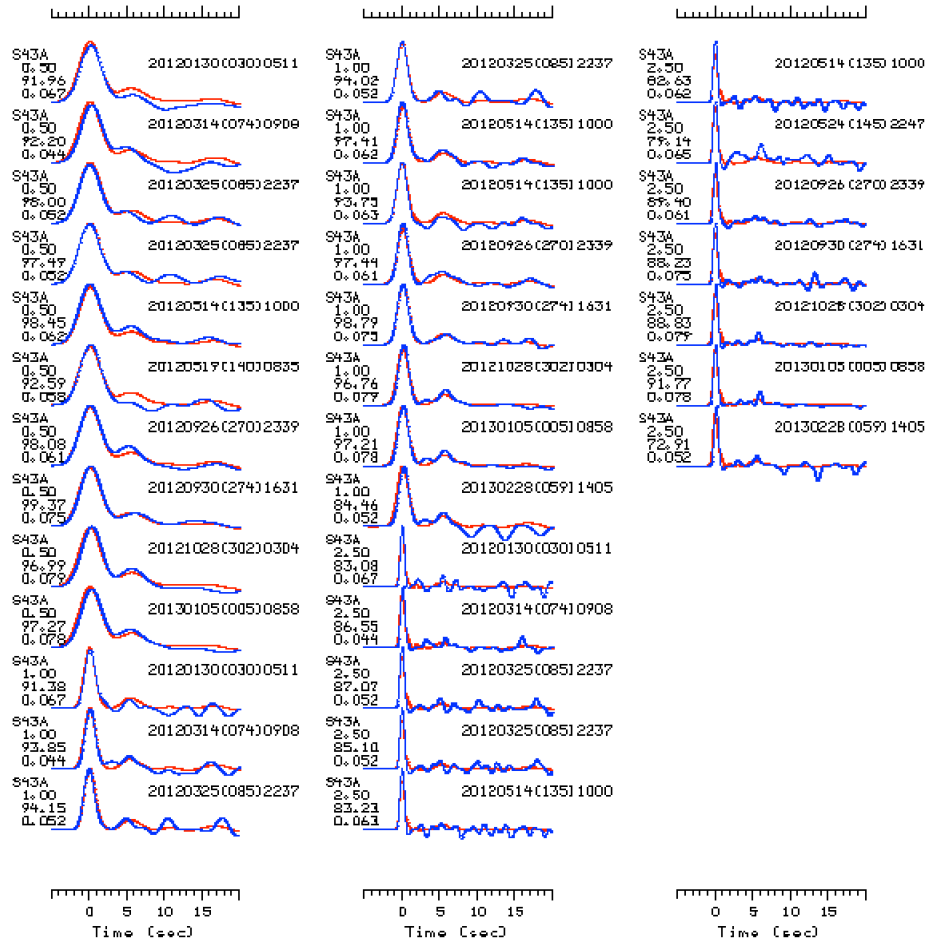


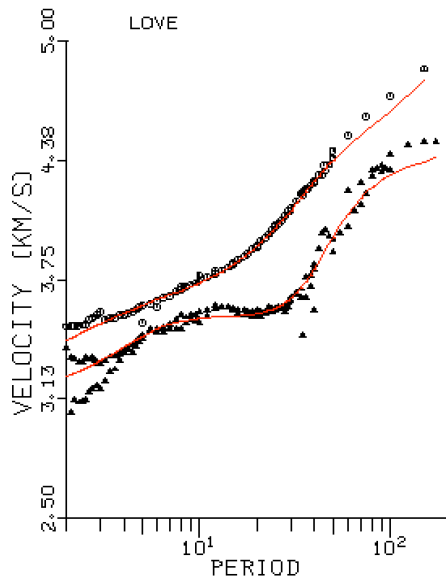
Figure 27: Velocity model and dataset before joint inversion under station S43A  
 (a) initial model (b) receiver function dataset (c) Love wave phase/group velocity dispersion  
 (d) Rayleigh wave phase/group velocity dispersion



(b)



(c)



(d)

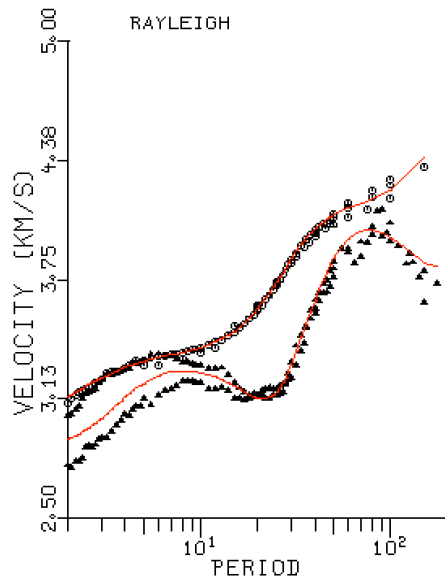


Figure 28: Velocity model and dataset before joint inversion under station S43A

- (a) initial model (b) receiver function dataset (c) Love wave phase/group velocity dispersion  
(d) Rayleigh wave phase/group velocity dispersion

*Note.* In (d), there are two datasets for the Rayleigh wave group velocity dispersion, and the red dispersion curve estimated from the final model fits the mean.

In Figure 27 (a), the initial model in red is also the model AK135. 33 receiver functions took part in the joint inversion (Figure 27 (b)). Before joint inversion, the predicted receiver functions (red) calculated with the initial model only match the first impulse of the observations (blue) at 0 second, while the second small impulse at about 5 seconds can't be detected in the predicted receiver functions (red). The mismatch between the prediction and observation is more obvious in the dispersion curves in Figure 27 (c, d). After 30-time iterative calculations, the tomographic model is obtained as the red curve in Figure 28 (a). The modification in velocity model makes the predicted receiver functions match both impulses of the observed data (Figure 28 (b)). The good match in receiver function and the similarity between the predicted and observed dispersion curves (Figure 28 (d)) indicate the accuracy of the final model.

### **5.3 2D Velocity profiles**

Another way to examine the subsurface structure is to construct 2D velocity profiles.

The velocity variation is presented to a 80 km depth in these profiles. Red to blue color means the velocity changing from slow to fast. Contours are marked at 3.4, 3.6, 3.8 4.0, 4.2 and 4.4 km/s. The locations of the stations are indicated above.

2D velocity profiles provide a better way to analyze the velocity variation of the shallow structure along a certain direction (see Figure 29). Take Figure 30(a) as an example. In the profile along line A-A', the Illinois basin can be found under stations Q43A to Q48A. The deepest part along this line is under station Q46A and depth of the basin can reach about 4 km.

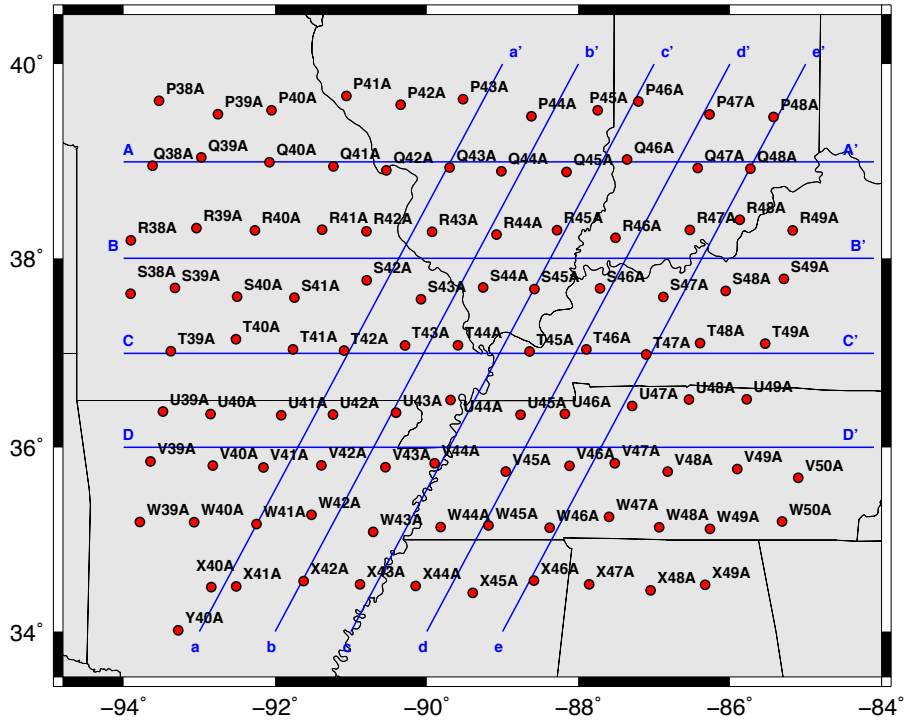
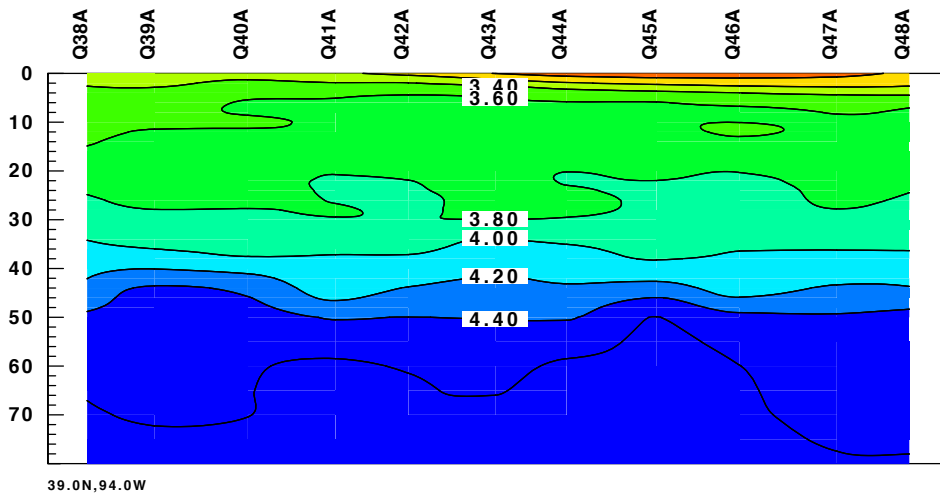
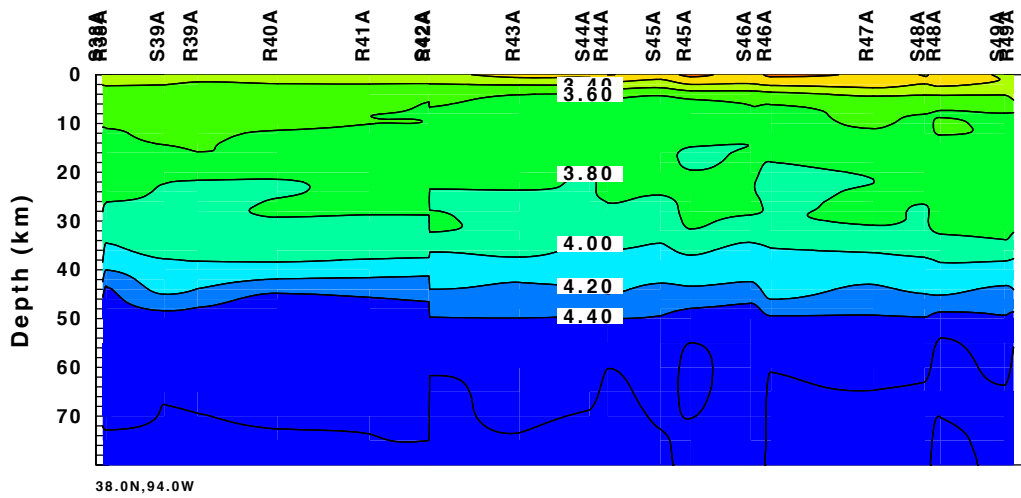


Figure 29: 2D Velocity profile lines

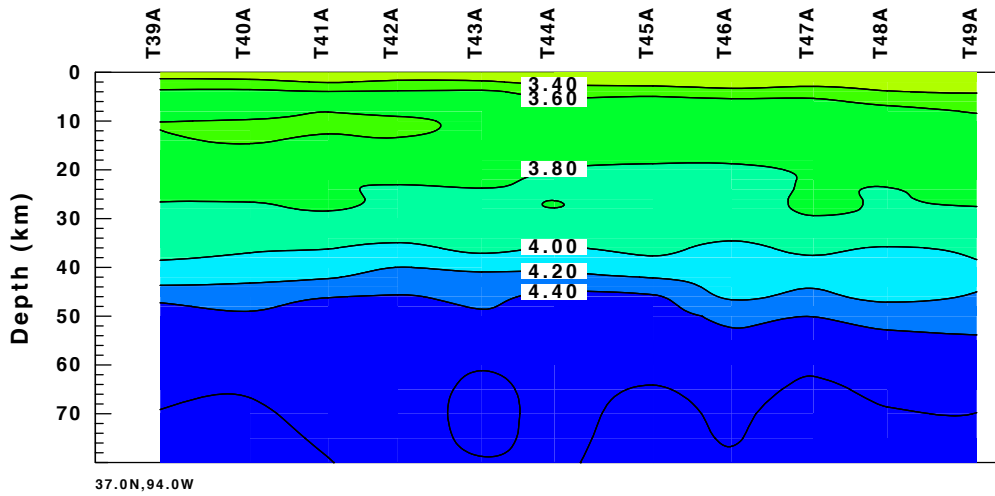
(a) A-A', 39N



(b) B-B', 38N



(c) C-C', 37N



(d) D-D', 36N

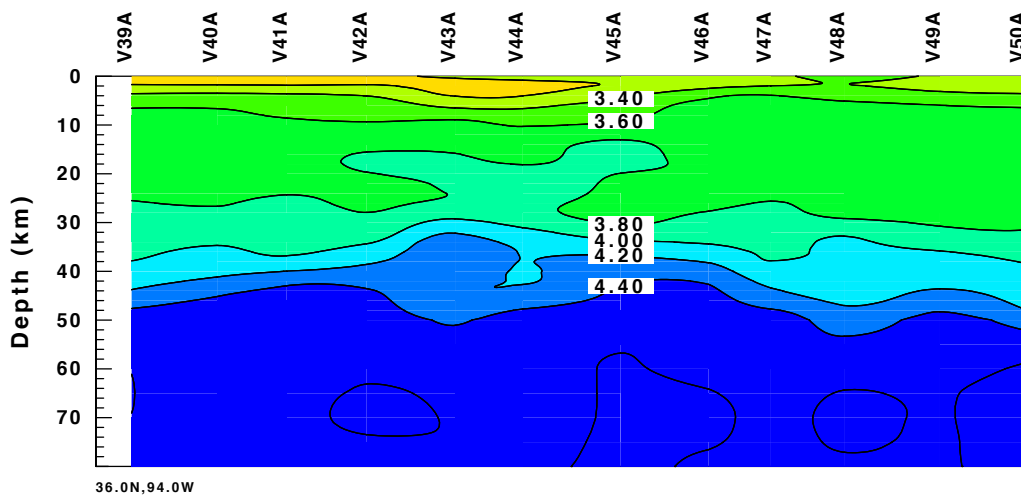
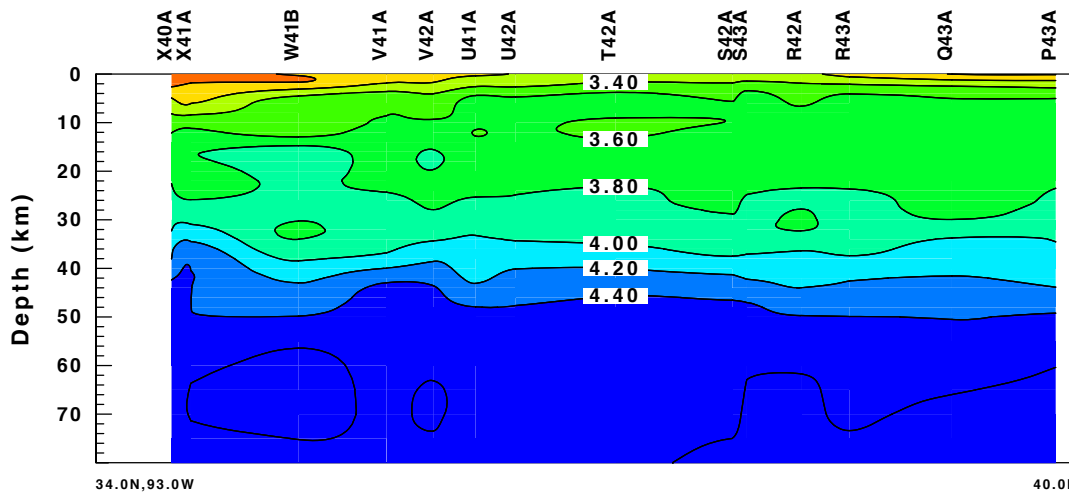
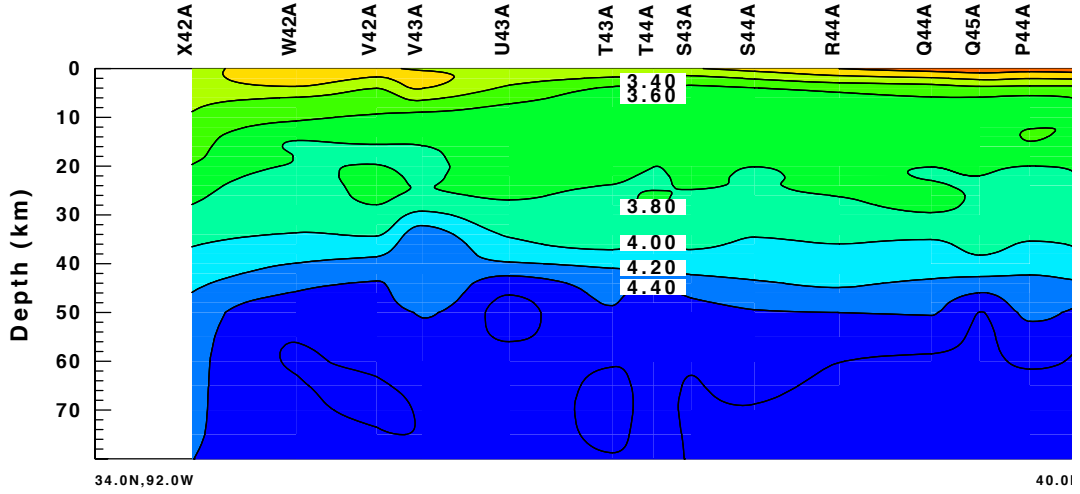


Figure 30: 2D east-west velocity profiles  
(a) A-A', 39N, (b) B-B', 38N, (c) C-C', 37N, (d) D-D', 36N

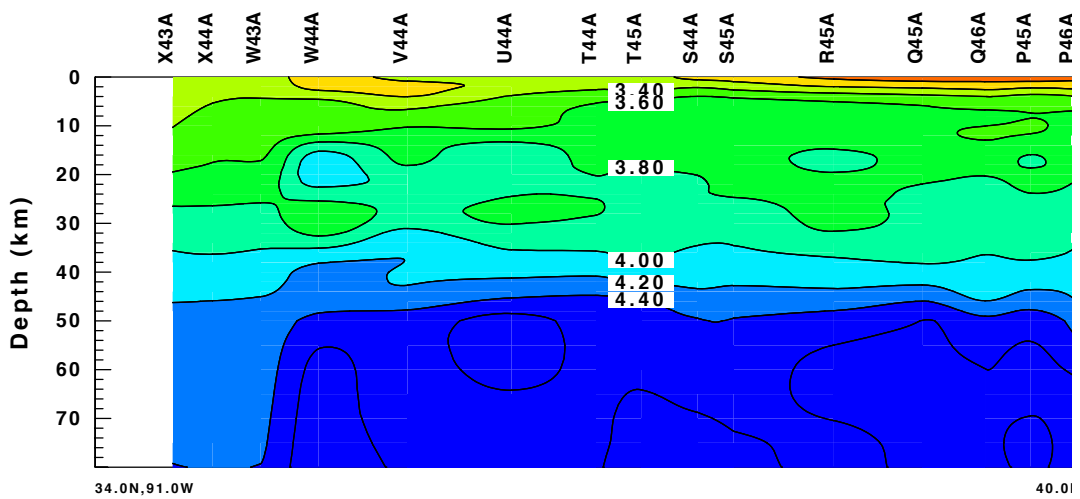
(a) a-a', (34N, 93W)–(40N, 90W)



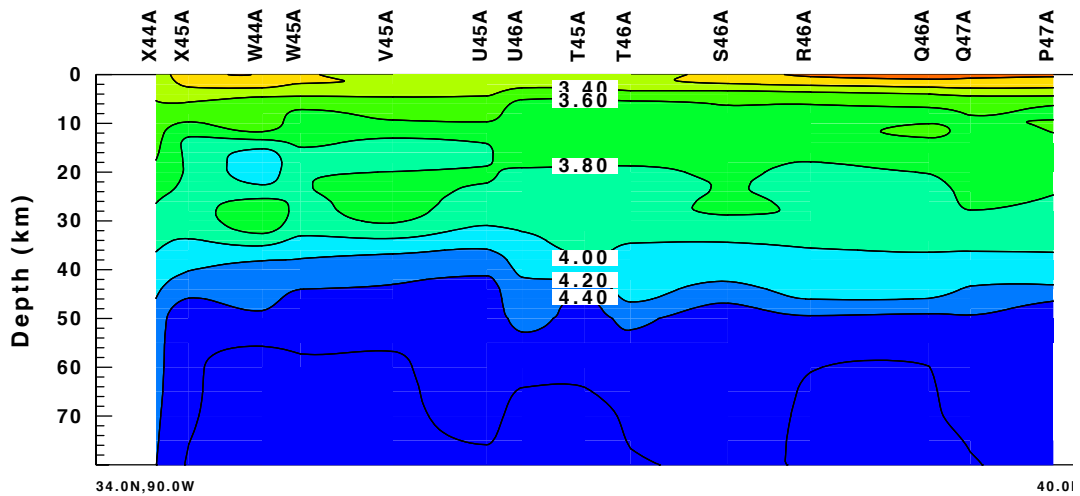
(b) b-b', (34N, 92W)–(40N, 89W)



(c) c-c', (34N, 91W)–(40N, 88W)



(d) d-d', (34N, 90W)–(40N, 87W)



(e) e-e', (34N, 89W)–(40N, 86W)

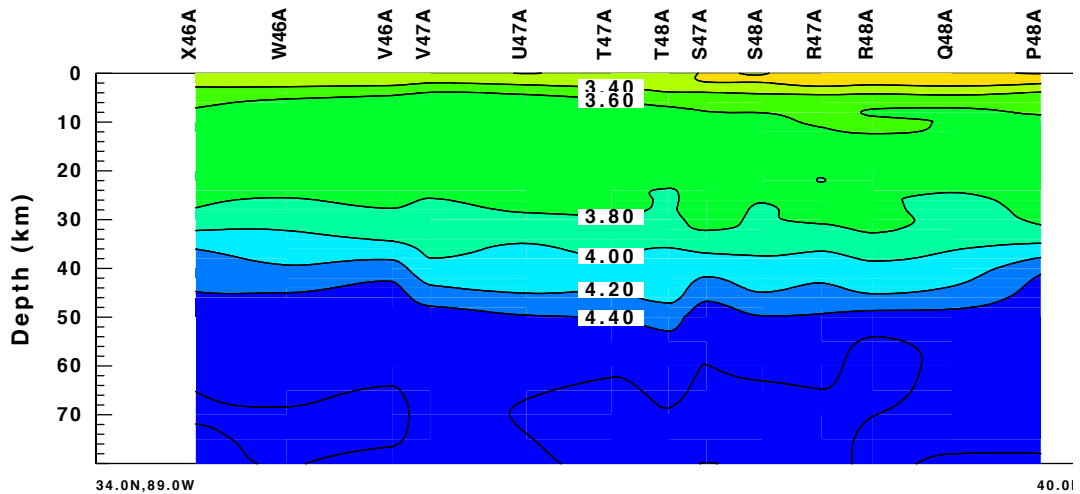


Figure 31: 2D velocity profiles paralleling the axis of embayment

- (a) a-a', (34N, 93W)–(40N, 90W), (b) b-b', (34N, 92W)–(40N, 89W),
- (c) c-c', (34N, 91W)–(40N, 88W), (d) d-d', (34N, 90W)–(40N, 87W),
- (e) e-e', (34N, 89W)–(40N, 86W)

#### 5.4 Model test

The constructed velocity models were tested to examine the reliability of our results.

A local earthquake event was occurred inside the study area, shown as a yellow star in Figure 32. Based on the result of a source inversion study, this event was happened in Missouri at 2011/06/07 08:10:34, with the magnitude of 3.86 and source depth of 27 km. Station Q42A and S43A recorded the seismic signals. By comparing the recorded and

synthetic waveforms calculated from different models, we are able to estimate if our model is close to the real underground structure, or which model is better.

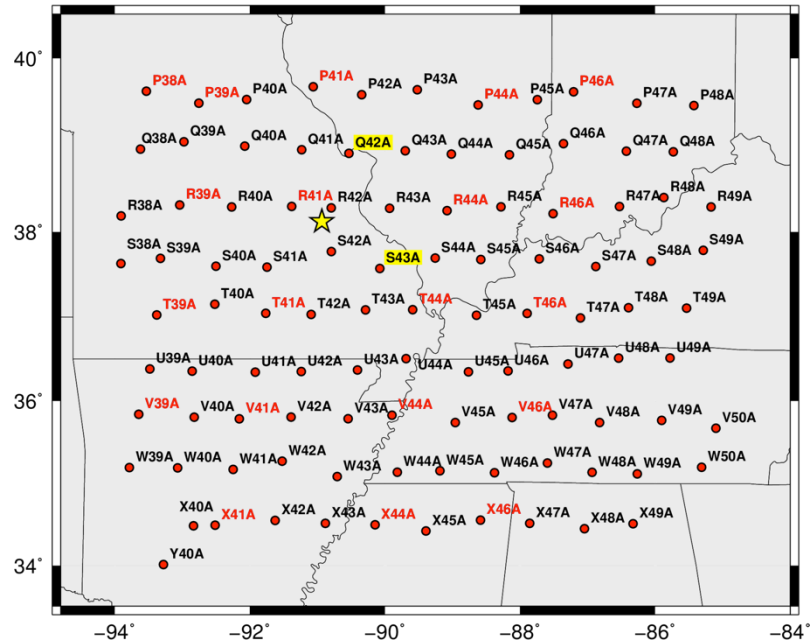


Figure 32: Model test map

Besides our resulting models under the station Q42A and S43A, we calculated the synthetics with other two models: one is the simple CUS model which has been mentioned in the section 5.1.3, the other is the HAM model [Herrmann and Ammon, 1997], which is modified from CUS model [Herrmann, 1979]. These models are plotted together in Figure 33. Note that the CUS model has an abrupt velocity change at 40 km, which corresponds to the Moho discontinuity, while the velocity change at the same depth for other models is smoother.

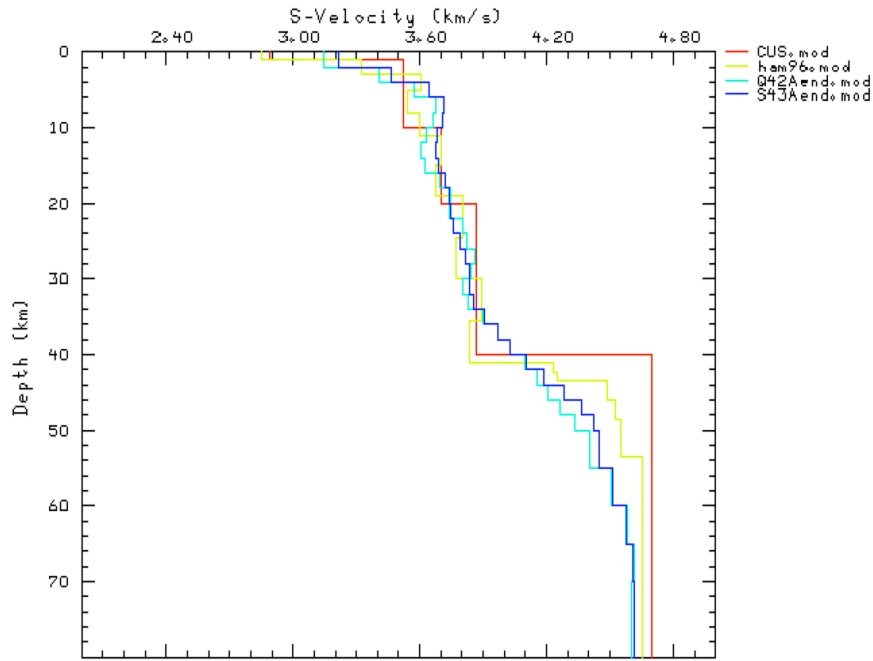


Figure 33: Models used for synthetics computation

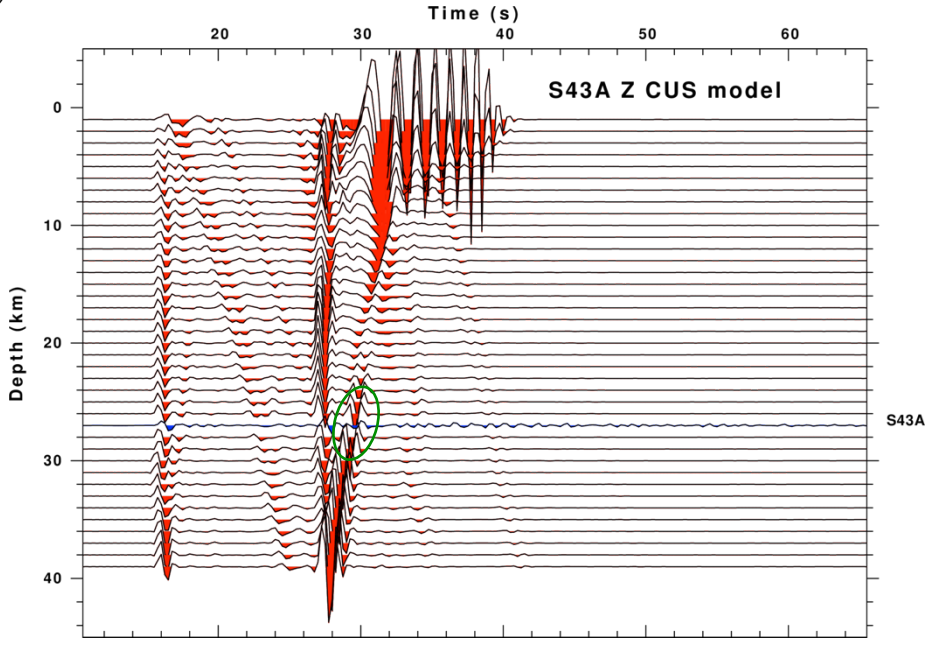
Although synthetic waveforms can be estimated with the source information and a known velocity model, it's not easy to compare the synthetics with the recorded waveform directly. The mismatch between the two waveforms may be attempting because it could be caused by other reasons than an inaccurate velocity model. For example, the mismatch might be caused by a wrong source depth, or the recorded waveform may be contaminated by noise which may not be recognized in single waveform comparison.

Thus, in this study, we used a series of source depths to calculate the waveforms and arranged the synthetics in the direction of increasing depth. Then we replaced the synthetic waveform estimated with source depth of 27 km with the recorded waveform. The match between the recorded waveform with the pattern of the synthetics is able to tell if the model used to calculate the synthetics can be regarded as a good approximation to the real velocity structure.

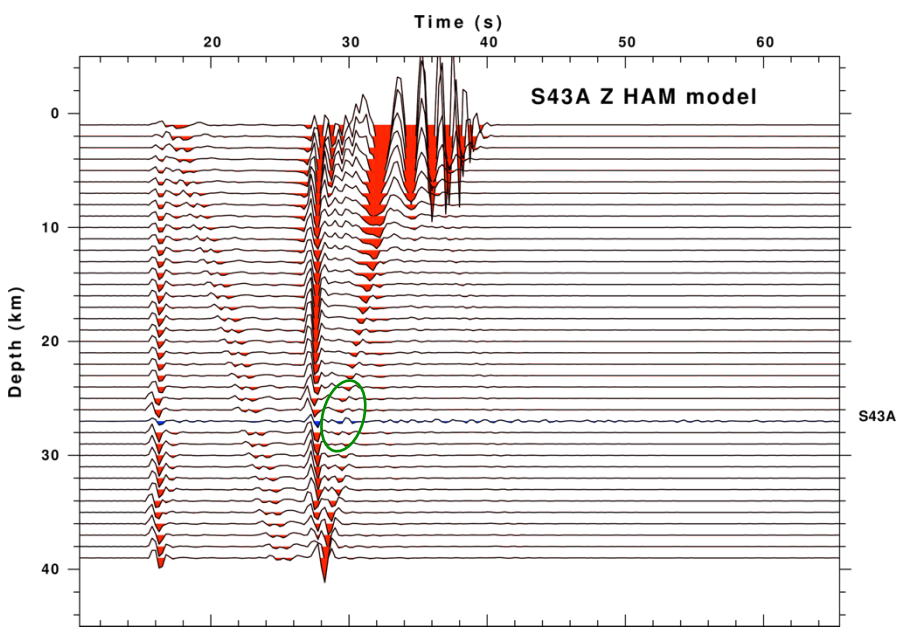
The two recorded time series at station S43A and Q42A are compared with the synthetics separately in Figure 34 and Figure 35. The recorded waveform is shown in blue

and other synthetics are shown in red. The green circles indicate the matching condition worth to be noted.

(a)



(b)



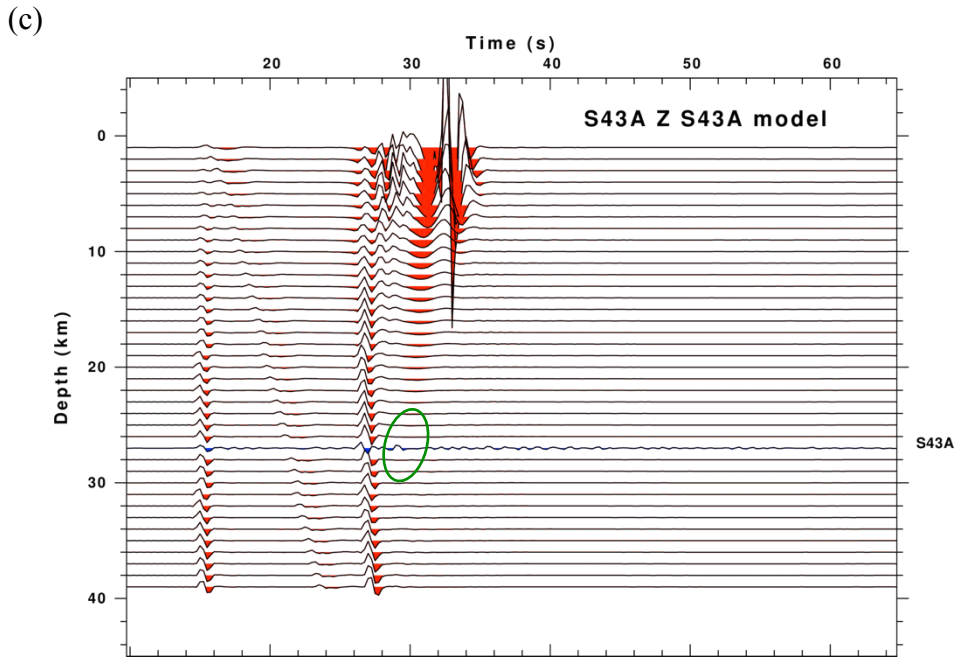
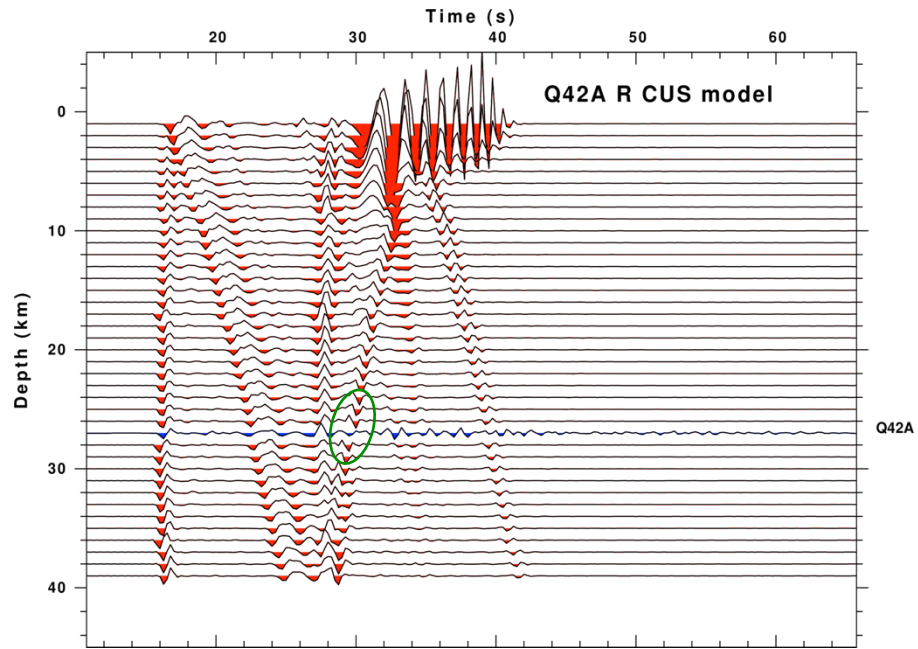


Figure 34: Waveform pattern comparison for station S43A.  
*Note.* Synthetics are estimated with (a) CUS model, (b) HAM model, (c) S43A model

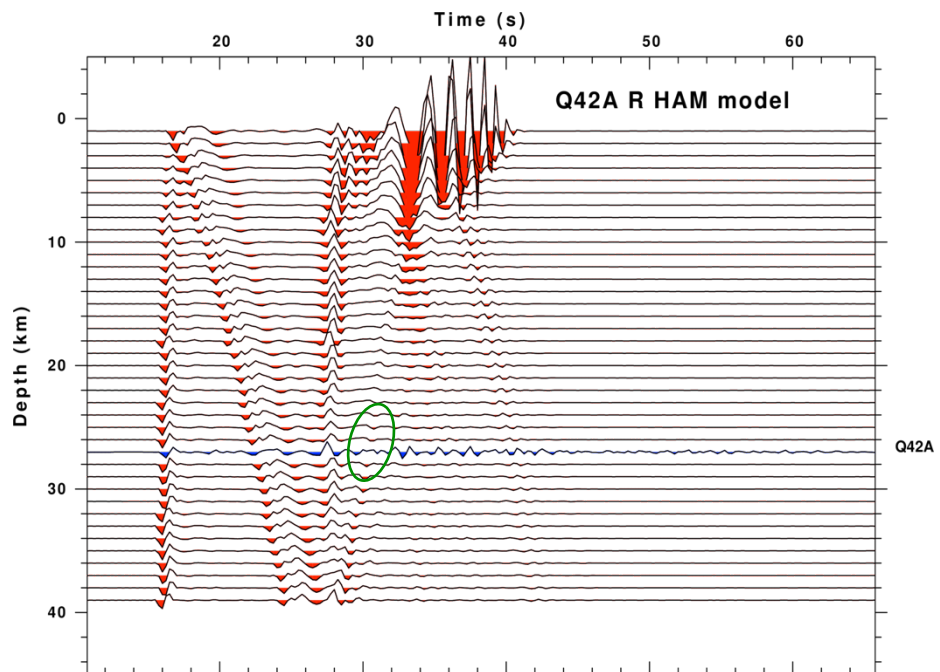
With different velocity models, the synthetics show different patterns. In Figure 34 (a), the synthetic waveforms were calculated at station S43A and based on the simple CUS model. The synthetic pattern shows a strong reflected S-wave, part of which is inside the green circle. And this strong phase is related to the sharp Moho boundary at 40 km in the CUS model. However, inside the green circle, the phase displayed in the observed record is found weaker than that in the surrounding synthetics.

Synthetics in Figure 34 (b) and (c) are computed with HAM model and our S43A model. Since both HAM model and our S43A model do not have an abrupt velocity increase at the 40 km depth as the CUS model (see Figure 33), no strong reflections are detected on the synthetic waveforms, which matches the weak phase on the observed record better.

(a)



(b)



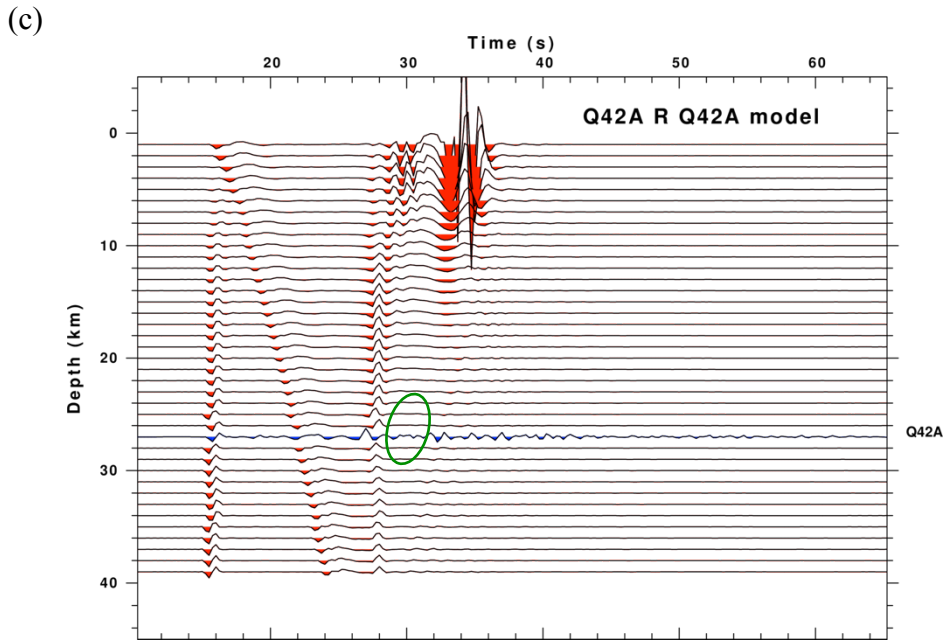


Figure 35: Waveform pattern comparison for station Q42A.

*Note.* Synthetics are estimated with (a) CUS model, (b) HAM model, (c) Q42A model

In the same way, a better fit between the synthetic pattern of HAM model, Q42A model and the observed waveform is observed in Figure 35. This fact leads to the conclusion that for the paths between the earthquake and these stations, the real subsurface velocity structure is closer to HAM and our models. Thus, instead of a sharp Moho boundary shown in CUS model, some locations in the study area are likely to have a gradient Moho at the depth of 40-60 km, as shown in HAM model and our models (see Figure 33).

## CHAPTER 6: CONCLUSION

In the northern ME, surface wave dispersion maps at periods of 2-50 seconds were obtained from ambient noise tomography. Compared to previous global or regional area tomography, the tomographic grid of our resulting dispersion maps has been improved from  $100 \text{ km} \times 100 \text{ km}$  to  $25 \text{ km} \times 25 \text{ km}$  for our study area. The resolved region estimated from checkerboard test is able to enclose the northern embayment. Checkerboard test also proved the effectiveness of the inversion program and raypath coverage.

In the real-data dispersion maps, the velocity perturbations agree with known tectonic features, e.g. the Illinois Basin in the NE and the Ozark uplift in the west. Compared with previous studies, the dispersion curves we obtained contain more short-period information with certain resolution. We consider the tomography work to be the major contribution of this study since it will form the basis for other studies.

Joint inversion of receiver functions and surface wave dispersion yields 1-D shear wave velocity models under each TA station within the study area. These S-velocity models display a similar behavior except for one deformed velocity model. The reason for this less constrained velocity model could be the limited receiver functions involved in joint inversion. In addition, the poor quality of receiver functions and surface wave data may also reduce the reliability of the resulting velocity structure.

It's interesting to find that both the 1-D velocity models and the model test results show that on some paths inside the study area, the nature of the Moho discontinuity is rather than the traditional sharp velocity change, but a gradient velocity increase within a certain depth range.

2-D velocity profiles have been created which provide a better way to show the velocity variation of the shallow structure along the east-west direction and the direction parallel to the axis of the embayment.

## REFERENCES

- Aki, K., and P. G. Richards (1980), *Quantitative Seismology: Theory and Methods*, San Francisco, CA.
- Al-Shukri, H. J., and B. J. Mitchell (1988), Reduced seismic velocities in the source zone of New Madrid earthquakes, *Bull. Seismol. Soc. Am.*, *78*(4), 1491-1509.
- Amante, C., and B. W. Eakins (2009), ETOPO1 1 Arc-Minute Global Relief Model: Procedures, Data Sources and Analysis, *NOAA Technical Memorandum NESDIS NGDC-24*, National Geophysical Data Center, NOAA, doi:10.7289/V5C8276M.
- Ammon, C. J. (1991), The isolation of receiver effects from teleseismic P waveforms, *Bull. Seismol. Soc. Am.*, *81*, 2504-2510.
- Ammon, C. J., G. E. Randall, and G. Zandt (1990), On the nonuniqueness of receiver function inversions, *J. Geophys. Res.*, *95*(B10), 15303-15318.
- Andrews, M. C., W. D. Mooney, and R. P. Meyer (1985), The relocation of microearthquakes in the northern Mississippi embayment, *J. Geophys. Res.*, *90*, 10223-10236.
- Bensen, G. D., M. H. Ritzwoller, M. P. Barmin, A. L. Levshin, F. Lin, M. P. Moschetti, N. M. Shapiro, and Y. Yang (2007), Processing seismic ambient noise data to obtain reliable broad-band surface wave dispersion measurements, *Geophys. J. Int.*, *169*(3), 1239-1260.
- Bensen, G. D., M. H. Ritzwoller, and N. M. Shapiro (2008), Broadband ambient noise surface wave tomography across the United States. *J. Geophys. Res.: Solid Earth (1978–2012)*, *113*, B05306, doi:10.1029/2007JB005248.

Bisrat, S., H. R. DeShon, and C. Rowe (2012), Microseismic swarm activity in the New Madrid seismic zone, *Bull. Seismol. Soc. Am.*, *102*(3), 1167-1178.

Braile, L. W., W. J. Hinze, G. R. Keller, E. G. Lidiak, and J. L. Sexton (1986), Tectonic development of the New Madrid rift complex, Mississippi embayment, North America, *Tectonophysics*, *131*(1), 1-21.

Braile, L. W., W. J. Hinze, and G. R. Keller (1997), New Madrid seismicity, gravity anomalies, and interpreted ancient rift structures, *Seism. Res. Lett.*, *68*(4), 599-610.

Calais, E., and S. Stein (2009), Time-variable deformation in the New Madrid Seismic Zone, *Science*, *323*, 1442, doi:10.1126/science.1168122.

Calais, E., G. Mattioli, C. DeMets, J. M. Nocquet, S. Stein, A. Newman, and P. Rydelek (2005), Seismology: Tectonic strain in plate interiors?, *Nature*, *438*, E9-E10, doi:10.1038/nature04428.

Catchings, R. D. (1999), Regional Vp, Vs, Vp/Vs and Poisson's ratios across earthquake source zones from Memphis, TN, to St. Louis, MO, *Bull. Seismol. Soc. Am.*, *89*, 1591-1605.

Chen, C., D. Zhao, and S. Wu (2014), Crust and upper mantle structure of the New Madrid Seismic Zone: Insight into intraplate earthquakes, *Physics of the Earth and Planetary Interiors*, *230*, 1-14, doi:10.1016/j.pepi.2014.01.016.

Chiu, J. M., G. Steiner, R. Smalley, and A. C. Johnston (1991), PANDA: a simple, portable seismic array for local-to regional-scale seismic experiments, *Bull. Seismol. Soc. Am.*, *81*(3), 1000-1014.

Chiu, J. M., A. C. Johnston, and Y. T. Yang (1992), Imaging the active faults of the central New Madrid seismic zone using PANDA array data, *Seism. Res. Lett.*, *63*, 375-393.

Cho, K. H., R. B. Herrmann, C. J. Ammon, and K. Lee (2007), Imaging the upper crust of the Korean Peninsula by surface-wave tomography, *Bull. Seismol. Soc. Am.*, 97(1B), 198-207.

Cox, R. T., and R. B. Van Arsdale (1997), Hotspot origin of the Mississippi embayment and its possible impact on contemporary seismicity, *Engineering Geology*, 46(3), 201-216.

Cox, R. T., and R. B. Van Arsdale (2002), The Mississippi Embayment, North America: a first order continental structure generated by the Cretaceous superplume mantle event, *Journal of Geodynamics*, 34, 163-176.

Cushing, E. M., E. H. Boswell, and R. L. Hosman (1964), General Geology of the Mississippi Embayment, U.S. *Geol. Surv. Prof. Pap. 448-B*, 28 pp..

Dart, R. L. (1995), Maps of upper Mississippi embayment Paleozoic and Precambrian rocks, *U.S. Geol. Surv. Misc. Field Stud. Map, MF-228*.

Dunn, M., H. R. DeShon, and C. A. Powell (2013), Imaging the New Madrid Seismic Zone using double-difference tomography, *J. Geophys. Res.: Solid Earth*, 118, 5404-5416, doi:10.1002/jgrb.50384.

Dziewonski, A. M., S. Bloch, and M. Landisman (1969), A technique for the analysis of transient seismic signals, *Bull. Seismol. Soc. Am.*, 59, 427-444.

Ekstrom, G. (2014), Love and Rayleigh phase-velocity maps, 5-40s, of the western and central USA from USArray data, *Earth Planet. Sci. Lett.*, 402, 42-49.

Ekstrom, G., J. Tromp, and E. W. F. Larson (1997), Measurements and global models of surface wave propagation, *J. Geophys. Res.*, 102, 8137-8157.

Elnashai, A. S., L. J. Cleveland, T. Jefferson, and J. HARRALD (2009), Impact of New Madrid Seismic Zone Earthquakes on the Central USA, *MAE Center Report No.09-03*, 139 pp., Mid-America Earthquake Center, Univ. of Illinois, IL.

Ervin, C. P., and L. D. McGinnis (1975), Reelfoot rift: Reactivated precursor to the Mississippi embayment, *Geol. Soc. Am. Bull.*, 86(9), 1287-1295.

Forte, A. M., J. X. Mitrovica, R. Moucha, N. A. Simons, and S. P. Grand (2007), Descent of ancient Farallon slab drives localized mantle flow below the New Madrid Seismic Zone, *Geophys. Res. Lett.*, 34, doi:10.1029/2006GL027895.

Ginsburg, A., W. D. Mooney, A. W. Walter, W. J. Lutter, and J. H. Healey (1983), Deep structure of northern Mississippi embayment, *AAPG Bulletin*, 67(11), 2031-2046.

Hatcher, R. D. Jr. (1989), Appalachian introduction, *The Geology of North America, F-2, Appalachian-Ouachita orogeny in the United States*, 1-6.

Herrmann, R. B. (1973), Some aspects of band-pass filtering of surface waves, *Bull. Seism. Soc. Am.*, 63, 663-671.

Herrmann, R. B. (1979), Surface wave focal mechanisms for eastern North American earthquakes with tectonic implications, *J. Geophys. Res.: Solid Earth (1978–2012)*, 84(B7), 3543-3552.

Herrmann, R. B. (2002), Computer programs in seismology, an overview of synthetic seismogram computation, Saint Louis University, St. Louis, MO.

Herrmann, R. B., and C. J. Ammon (1997), Faulting parameters of earthquakes in the New Madrid, Missouri region, *Engineering Geology*, 46, 299-311.

Herrmann, R. B., and C. J. Ammon (2002), Computer programs in seismology, surface waves, receiver functions and crustal structure, Saint Louis University, St. Louis, MO.

Herrmann, R. B., and G. W. Fischer (1978), Theoretical seismogram constraints on some crustal velocity models in the central United States, *Pure Appl. Geophys.*, *116*(6), 1250-1261.

Herrmann, R. B., H. Benz, and C. J. Ammon (2011), Monitoring the earthquake source process in North America, *Bull. Seismol. Soc. Am.*, *101*(6), 2609-2625.

Hildenbrand, T. G. (1985), Rift structure of the northern Mississippi embayment from the analysis of gravity and magnetic data, *J. Geophys. Res.*, *90*, doi: 10.1029/JB080i015p12607.

Hildenbrand, T. G., and J. D. Hendricks (1995), Geophysical setting of the Reelfoot Rift and relations between rift structures and the New Madrid seismic zone, *U.S. Geol. Surv. Prof. Pap.* *1538-E*, 1-30.

Hildenbrand, T. G., and R. W. Johnson (1977), Aeromagnetic map of the northern Mississippi Embayment, parts of Missouri, Arkansas, Tennessee, and Kentucky, *Open File Rep.* *77-229*, U.S. Geol. Surv., Denver, CO.

Hildenbrand, T. G., C. P. Ervin, J. Hendricks, G. R. Keller, L. D. McGinnis, and R. G. Stearns (1977a), Bouguer gravity map of the northern Mississippi Embayment, part of Missouri, Arkansas, Tennessee, Kentucky, and Illinois, *Open File Rep.* *77-228*, U.S. Geol. Surv., Denver, CO.

Hildenbrand, T. G., M. F. Kane, and W. Stauder (1977b), Magnetic and gravity anomalies in the northern Mississippi embayment and their spatial relation to seismicity, *Map MF-914*, U.S. Geol. Surv., Reston, VA.

Hildenbrand, T. G., M. F. Kane and J. D. Hendricks (1982), Magnetic basement in the upper Mississippi Embayment region - a preliminary report, investigations of the New Madrid, Missouri, earthquake region, *U.S. Geol. Surv. Prof. Pap. 1236*, 39-53.

Hinze, W. J., and L. W. Braile (1988), Geophysical aspects of the craton: U.S., in *Sedimentary cover: North American craton; U.S., The Geology of North America*, vol. D-2, edited by L. L. Sloss, pp. 5-24, Geological Society of America, Boulder, Colorado.

Jin, G., and J. B. Gaherty (2015), Surface wave phase-velocity tomography based on multichannel cross-correlation, *Geophys. Jour. Inter.*, *201*(3), 1383-1398.

Johnston, A. C., and E. S. Schweig (1996), The enigma of the New Madrid earthquakes of 1811-1812, *Annu. Rev. Earth Planet. Sci.*, *24*(1), 339-384.

Julia, J., C. J. Ammon, R. B. Herrmann, and A. M. Correig (2000), Joint inversion of receiver function and surface wave dispersion observations, *Geophys. Jour. Inter.*, *143*(1), 99-112.

Kane, M. F., T. G. Hildenbrand, and J. D. Hendricks (1981), A model for the tectonic evolution of the Mississippi Embayment and its contemporary seismicity, *Geology*, *9*(12), 563-568.

Kennett, B. L. N., E. R. Engdahl, and R. Buland (1995), Constraints on seismic velocities in the Earth from traveltimes, *Geophys. Jour. Inter.*, *122*(1), 108-124.

Kikuchi M., and H. Kanamori (1982), Inversion of complex body waves, *Bull. Seismol. Soc. Am.*, *72*(2), 491-506.

Langston, C. A. (1979), Structure under Mount Rainier, Washington, inferred from teleseismic body waves, *J. Geophys. Res.*, *84*, 4749-4762.

Langston, C. A. (1994), An integrated study of crustal structure and regional wave propagation for southeastern Missouri, *Bull. Seismol. Soc. Am.*, 84(1), 105-118.

Larson, E. W. F., and G. Ekstrom, (2001), Global models of surface wave group velocity, *Pure Appl. Geophys.*, 158(8), 1377-1399.

Levshin, A. L. (1973), Surface and channel seismic waves, 176 pp., Nauka, Moscow.

Liang, C., and C. A. Langston (2008), Ambient seismic noise tomography and structure of eastern North America, *J. Geophys. Res.: Solid Earth (1978–2012)*, 113(B3), B03309, doi:10.1029/2007JB005350.

Ligorria, J., and C. Ammon (1999), Iterative deconvolution and receiver- function estimation, *Bull. Seismol. Soc. Am.*, 89(5), 1395-1400.

Lin, F. C., M. P. Moschetti, and M. H. Ritzwoller (2008), Surface wave tomography of the western United States from ambient seismic noise: Rayleigh and Love wave phase velocity maps, *Geophys. Jour. Inter.*, 173(1), 281-298.

Long, M. D., A. Levander, and P. M. Shearer (2014), An introduction to the special issue of Earth and Planetary Science Letters on USArray science, *Earth Planet. Sci. Lett.*, doi:10.1016/j.epsl.2014.06.016.

Lowrie, W. (2007), Fundamentals of Geophysics, 2nd ed., 381 pp., Cambridge Univ. Press, New York.

Mooney, W. D., M. C. Andrews, A. Ginzburg, D. A. Peters, and R. M. Hamilton (1983), Crustal structure of the northern Mississippi Embayment and comparison with other continental rift zones, *Tectonophysics*, 94, 327–348.

Mooney, W. D., and M. C. Andrews (1984), Seismic refraction studies of the Mississippi embayment, in Proceedings of the Symposium on the New Madrid Seismic Zone, *U.S. Geol. Surv. Open File Rep. 84-770*, 138-167.

Mordret, A., M. Landès, N. M. Shapiro, S. C. Singh, and P. Roux (2014), Ambient noise surface wave tomography to determine the shallow shear velocity structure at Valhall: depth inversion with a Neighbourhood Algorithm, *Geophys. Jour. Inter.*, 198(3), 1514-1525.

Moschetti, M. P., M. H. Ritzwoller, and N. M. Shapiro (2007), Surface wave tomography of the western United States from ambient seismic noise: Rayleigh wave group velocity maps, *Geochem., Geophys., Geosys.*, 8, Q08010, doi:10.1029/2007GC001655.

Nelson, K. D., and J. Zhang (1991), A COCORP deep reflection profile across the buried Reelfoot rift, south-central United States, *Tectonophysics*, 197, 271–293.

Newman, A., S. Stein, J. Weber, J. Engeln, A. Mao, and T. Dixon (1999), Slow deformation and lower seismic hazard at the New Madrid seismic zone, *Science*, 284(5414), 619-621.

Nuttli, O. W. (1973), The Mississippi Valley earthquakes of 1811 and 1812: Intensities, ground motion and magnitudes, *Bull. Seismol. Soc. Am.*, 63(1), 227-248.

Owens, T. J., G. Zandt, and S. R. Taylor (1984), Seismic evidence for an ancient rift beneath the Cumberland Plateau, Tennessee: a detailed analysis of broadband teleseismic P waveforms, *J. Geophys. Res.*, 89, 7783-7795.

Ozalaybey, S., M. K. Savage, A. F. Sheehan, J. N. Louie, and J. N. Brune (1997), Shear-wave velocity structure in the northern Basin and Range province from the combined analysis of receiver functions and surface waves, *Bull. Seismol. Soc. Am.*, 87(1), 183-199.

Pollitz, F. F., and J. A. Snoke (2010), Rayleigh-wave phase-velocity maps and three dimensional shear-velocity structure of the western US from local non-plane surface-wave tomography, *Geophys. J. Int.*, *180*, 1153–1169.

Powell, C. A., M. M. Withers, H. R. DeShon, and M. M. Dunn (2010), Intrusions and anomalous Vp/Vs ratios associated with the New Madrid seismic zone, *J. Geophys. Res.*, *115*, B08311, doi:10.1029/2009JB007107.

Pollitz, F. F., and W. D. Mooney (2014), Seismic structure of the Central US crust and shallow upper mantle: Uniqueness of the Reelfoot Rift, *Earth Planet. Sci. Lett.*, *402*, 157-166.

Reed., J. C. Jr., J. O. Wheeler, and B. E. Tucholke (2004), Geologic map of North America: Decade of North American Geology Continental Scale Map 001, Boulder, Geological Society of America, scale 1:5,000,000.

Saucier, R. T., and J. I. Snead (1989), Quaternary geology of the lower Mississippi valley: Louisiana Geological Survey, Quaternary Nonglacial Geology: Conterminous U.S. Vol. K-2 of The Geology of North America (GNA-K2) Plate 6.

Shapiro, N. M., and M. Campillo (2004), Emergence of broadband Rayleigh waves from correlations of the ambient seismic noise, *Geophys. Res. Lett.*, *31*(7), L07614.

Shapiro, N. M., M. Campillo, L. Stehly, and M. H. Ritzwoller (2005), High-resolution surface-wave tomography from ambient seismic noise, *Science*, *307*(5715), 1615-1618.

Shedlock, K. M., and A. C. Johnston (1994), Investigations of the New Madrid Seismic Zone, *U.S. Geol. Surv. Prof. Pap.* 1538-FG.

Shen, W., M. H. Ritzwoller, and V. Schulte-Pelkum (2013), A 3-D model of the crust and uppermost mantle beneath the Central and Western US by joint inversion of receiver functions and surface wave dispersion, *J. Geophys. Res.: Solid Earth*, 118(1), 262-276.

Snieder, R. (2004), Extracting the Green's function from the correlation of coda waves: A derivation based on stationary phase, *Physical Review E*, 69(4), 046610.

Stearns, R. G. (1957), Cretaceous, Paleocene, and lower Eocene geologic history of the northern Mississippi embayment, *Geol. Soc. Am. Bull.*, 68(9), 1077-1100.

Stearns, R. G., and M. V. Marcher (1962), Late Cretaceous and subsequent structural development of the northern Mississippi embayment area, *Geol. Soc. Am. Bull.*, 73(11), 1387-1394.

Tuttle, M. P., E. S. Schweig, J. D. Sims, R. H. Lafferty, L. W. Wolf, and M. L. Haynes (2002), The earthquake potential of the New Madrid seismic zone, *Bull. Seismol. Soc. Am.*, 92(6), 2080-2089.

Tuttle, M. P., H. Al-Shukri, and H. Mahdi (2006), Very large earthquakes centered southwest of the New Madrid seismic zone 5,000-7,000 years ago, *Seism. Res. Lett.*, 77(6), 664-678.

Van Arsdale, R. B., and R. K. TenBrink (2000), Late Cretaceous and Cenozoic geology of the New Madrid seismic zone, *Bull. Seismol. Soc. Am.*, 90(2), 345-356.

Vlahovic, G., and C. A. Powell (2001), Three-dimensional S wave velocity structure and Vp/Vs ratios in the New Madrid Seismic Zone. *J. Geophys. Res.: Solid Earth (1978–2012)*, 106(B7), 13501-13513.

Vlahovic, G., C. A. Powell, and J. M. Chiu (2000), Three-dimensional P wave velocity structure in the New Madrid seismic zone, *J. Geophys. Res.: Solid Earth (1978–2012)*, *105*(B4), 7999-8011.

Wapenaar, K. (2004), Retrieving the elastodynamic Greens function of an arbitrary inhomogeneous medium by cross correlation, *Phys. Rev. Lett.*, *93*, 254301-1 - 254301-4.

Zhang, Q., E. Sandvol, and M. Liu (2009), Lithospheric velocity structure of the New Madrid Seismic Zone: A joint teleseismic and local P tomographic study, *Geophys. Res. Lett.*, *36*(11).

Zhu, L., and H. Kanamori (2000), Moho depth variation in southern California from teleseismic receiver functions, *J. Geophys. Res. B*, *105*(B2), 2969-2980.

Zoback, M. D., R. M. Hamilton, A. J. Crone, D. P. Russ, F. A. McKeown, and S. R. Brockman (1980), Recurrent intraplate tectonism in the New Madrid seismic zone, *Science*, *209*, 971-976.

## **VITA AUCTORIS**

Han Su was born in 1991 in Hebei, China. In 2009, She was graduated from Baoding Foreign Language School. At the same year, she was admitted to Southwest Petroleum University where she obtained a Bachelor of Science degree in Exploration Geophysics in 2013. Now, she is a master student at the Saint Louis University, St. Louis, MO, US. She has been working on the project, Lithospheric Structure Beneath Northern Mississippi Embayment from Joint Inversion of Surface Wave Dispersion and Receiver Functions, with her supervisor, Dr. Robert Herrmann, for the past two years. She is going to graduate in the summer of 2015 with a Master of Science degree in Geophysics.